Light Scattering on Partially Absorbing Homogeneous Spheres of Finite Size

D. Deirmendjian and R. J. Clasen

February 1962

R-393-PR

A REPORT PREPARED FOR

UNITED STATES AIR FORCE PROJECT RAND

The RAND Corporation
1700 MAIN ST • SANTA MONICA • CALIFORNIA

SUMMARY

THIS REPORT presents a partial description and a discussion of the quantitative results based on the exact solution of the following theoretical problem: For a sphere of arbitrary size, composed of homogeneous material with a finite dielectric constant and conductivity, receiving a constant flux of energy from a single direction in the form of plane electromagnetic waves of a given frequency and state of polarization, find the total amount of energy absorbed and scattered by the sphere, as well as the specific intensity and the state of polarization of the energy scattered in a given direction, at a large distance from the sphere. A complete analytical solution to this problem was obtained some time ago by Gustav Mie on the basis of Maxwellian field theory. The present study gives accurate numerical results, based on Mie's expressions, for a wide range of basic parameters not treated earlier. Illustrated and discussed by means of selected examples are the effects of variations in dielectric and conducting properties on the total scattering and absorption cross sections as a function of the relative size of the sphere, as well as on the differential amplitude, intensity, and polarization of the scattered energy.

The work was undertaken as a preliminary and necessary step in a general study of planetary atmospheres containing particles of various sizes and types, whose characteristics are to be determined by means of the reflected and transmitted visible and infrared sunlight. The results, after proper scaling, are equally applicable to spheres receiving electromagnetic radiations of much lower frequencies, such as microwaves.

PREFACE

THE MAIN RESULTS of this work have appeared in D. Deirmendjian, R. Clasen, and W. Viezee, "Mie Scattering with Complex Index of Refraction," *J. Opt. Soc. Am.*, Vol. 51, No. 6, June, 1961, pp. 620–633. The minor errors in the curves in Figs. 6, 7, 9, and 10, noted in that publication, have been corrected in the corresponding figures of the present report.

The authors are indebted to Professor Zdenek Sekera for many valuable suggestions and to Mr. William Viezee (now at Stanford Research Institute, Menlo Park, California) for assisting in numerical checks of the computational formulas and for plotting some of the initial results.

CONTENTS

INTRODUCTION

IN RECENT YEARS an increasing number of computations and tables related to the scattering of light on homogeneous dielectric spheres have appeared in the literature. A comprehensive list and an evaluation of these appear in van de Hulst's authoritative monograph.[1] Since the publication of his study in 1957, additional work has been done, but in most of the published material, only the total scattering cross section is listed, together with individual Mie coefficients, for the case of nonabsorbing spheres of various sizes and indices of refraction. The amplitude and intensity of the scattered light as a function of scattering angle are usually omitted.†

A complete knowledge of the intensity and polarization of light that has been scattered in various directions is essential in understanding the role of large particles, such as aerosol and cloud particles, in the radiative transfer of visible and infrared light in atmospheres containing such particles. Moreover, a consideration of dielectric spheres alone is not sufficient. For example, it has been shown[2][3] that in the scattering of infrared radiation by cloud particles, a complex index of refraction is appropriate, since water and ice display infrared absorption bands. An understanding of the scattering and absorption of ultraviolet, visible, and infrared light by partially absorbing particles is also important in problems presented by sunlit planetary atmospheres other than our own, as well as by interplanetary and interstellar particles of a size comparable to the wavelength.[1][4]

We might sketch the extent of present knowledge of the scattering mechanism (more fully described by van de Hulst,[1] Twersky,[5] and others) as follows: The particles, assumed spherical, are characterized by two parameters, x and m. The size parameter, x, is the product of the free-space propagation constant, k, and the radius, a, of the sphere. The complex index of refraction m is related to the dielectric constant and to the conductivity of the substance. Using these two parameters, we may classify the types of scattering into the following principal cases.

† These remarks do not apply to the literature appearing after March, 1961.

RAYLEIGH SCATTERING

Rayleigh scattering is restricted to the case $x << 1$, but m is arbitrary. This limiting case, applied to a purely molecular atmosphere, successfully explains most observed features of the color, the intensity, and the polarization of the sunlit sky. It is also applicable to problems of radar backscatter from cloud and rain droplets, provided their dimensions are sufficiently small compared with the wavelength.

RAYLEIGH–GANS SCATTERING

In Rayleigh–Gans scattering we have $|m-1| << 1$ and $2x|m-1| << 1$. This is a limited extension of the Rayleigh case. The conditions are more stringent, in that the properties of the sphere must differ only slightly from those of the surrounding medium. The restrictions on size, however, are less stringent than in the Rayleigh scattering described in the preceding section, since the case $x > 1$ can be treated, provided the second condition above is satisfied. The approach is useful in treating the radar backscatter from cloud and rain. Furthermore, such nonspherical particles as cylinders and elipsoids can be considered, where the radius of a sphere is replaced by another characteristic dimension.

VAN DE HULST APPROXIMATION

The van de Hulst approximation is restricted to $|m-1| << 1$, but x may be arbitrary. This approximation has proved most successful in predicting the total extinction cross section and its dependence on the size of the spheres. The theory is less successful in the case of absorbing spheres. Essentially, the same type of approximation is involved in what is known as the W.K.B. approach, which describes the angular scattering and polarization as well, within small angles of scattering. The theory and applications have been discussed in Refs. 3 and 6 through 9. Methods of improving the approximation have been discussed by Sekera in Ref. 10. The method so far fails to give a correct estimate of the intensity and polarization at large angles of scattering, particularly in the backward hemisphere.

GEOMETRIC-OPTICS LIMIT

The geometric-optics case corresponds to $x \to \infty$ with m real and either finite or infinite. This case is equivalent to a wavelength that is infinitesimal compared with the size of the scatterer, and independent rays of light can be analyzed as they enter and leave the

medium. The pattern of the scattered light is assumed to be given by effects of refraction, reflection, and diffraction. This approach has provided us with qualitative explanations of ordinary rainbows, diffraction patterns, and halos, produced by cloud and rain droplets. It fails to explain the total cross sections, the polarization observed in the rainbow, and other quantitative details in the scattered pattern, because important mechanisms, such as contributions from surface waves and internal losses cannot be easily considered.

ELECTROMAGNETIC THEORY—MIE SCATTERING

In this instance both m (complex) and x may be arbitrary. For the case of *spheres*, Mie solved a boundary-value problem using Maxwell's electromagnetic theory. The solution is exact, and it describes the field both inside and outside a sphere for any scattering angle, size, and index of refraction. At the limits $x << 1$ and $x \to \infty$, it gives the known features of the Rayleigh and geometric-optics approximations. Because the exact theory is most useful between these limits, problems in this range are usually referred to as Mie scattering problems and the corresponding particles as Mie particles. This is the theory on which the present computations are based.

Calculations of Mie scattering with *complex index*, especially for spheres of finite relative size x, are rather scarce. The work of Schoenberg and Jung, that of Schalen, and Mie's original computations, as described by van de Hulst,[1] generally involve small spheres (less than one wavelength in diameter), so that a series expansion in x may be used.[11] For larger spheres, we have a few limited cases given in Lowan's tables.[12] In addition, values of the extinction cross section alone, based on the Mie theory, are given by Johnson and Terrell,[2] and by Haugen.[13]

The purpose of this report is to describe new and more detailed computations, performed at The RAND Corporation, of the scattering and absorption characteristics of spheres of various optical properties, mainly corresponding to liquid water illuminated by visible and infrared radiation. Examples are presented mostly by means of suitable plots of the functions.

NOTATION AND COMPUTATIONAL SCHEME

THE MATHEMATICAL FORMALISM relating to the Mie theory will be kept to a minimum, by referring the reader to van de Hulst's clear and consistent discussion.† With minor variations, we adopt the symbols and definitions introduced by that author. In brief, we are given the following: the size parameter, $x = ka$, where $k = 2\pi/\lambda$ and $\lambda =$ the free-space wavelength of the incident radiation; $m = r - ir'$, the complex index of refraction in the interior of the sphere with respect to the medium, where $m = (\varepsilon - 4\pi i\sigma/\omega)^{1/2}$, ε being the dielectric constant, σ the conductivity, and ω the circular frequency of the electromagnetic wave; and the scattering angle θ measured from the forward direction.

The incident plane-wave radiation is assumed unpolarized so that the electric field may be represented by two independent and mutually perpendicular oscillations of unit amplitude in the form

$$E = e^{-i(kz+\omega t)}$$

propagating in the direction z. The resultant field will be the sum of the initial field plus a scattered field, whose electric amplitude may be expressed in the form of two vector components, A_1 perpendicular to the scattering plane (in which the scattering angle θ is measured) and A_2 parallel to the scattering plane. At large distances from the sphere, in the so-called radiation limit, these vectors have no component along the direction of propagation. According to the Mie theory,[1] the magnitude of these far-field amplitude vectors may be expressed in dimensionless form as follows:

$$kA_1 \equiv S_1(x, m, \theta) = \sum_{n=1}^{\infty} \frac{2n+1}{n(n+1)} \{a_n\pi_n + b_n\tau_n\}, \tag{1}$$

$$kA_2 \equiv S_2(x, m, \theta) = \sum_{n=1}^{\infty} \frac{2n+1}{n(n+1)} \{b_n\pi_n + a_n\tau_n\}, \tag{2}$$

†See pp. 114*ff*. of Ref. 1.

$$K_{ext}(x, m) = \frac{2}{x^2} \sum_{n=1}^{\infty} (2n + 1) \operatorname{Re} \{a_n + b_n\}, \tag{3}$$

and

$$K_{sc}(x, m) = \frac{2}{x^2} \sum_{n=1}^{\infty} (2n + 1) \{ |a_n|^2 + |b_n|^2 \} \tag{4}$$

where S_1 and S_2 are the dimensionless complex amplitude functions; K_{ext} and K_{sc} are the total extinction and scattering cross sections divided by the geometrical cross section (called the "efficiency factors" Q_{ext} and Q_{sc} in van de Hulst's treatment); $a_n(m, x)$ and $b_n(m, x)$ are the Mie complex scattering coefficients; and $\pi_n(\theta)$ and $\tau_n(\theta)$ are the angle-dependent coefficients

$$\left.\begin{aligned} \pi_n(\mu) &= \frac{d}{d\mu} P_n(\mu), \\ \tau_n(\mu) &= \mu\pi_n(\mu) - (1 - \mu^2) \frac{d}{d\mu} \pi_n(\mu), \end{aligned}\right\} \quad -1 \leqq \mu \leqq 1,$$

where $\mu = \cos\theta$ and $P_n(\mu)$ is the Legendre polynomial of order n.

The most troublesome quantities to treat computationally are the coefficients a_n and b_n, since they involve spherical Bessel functions of real and complex arguments. However, the corresponding expressions may be written in terms of ordinary Bessel functions of the first kind, of orders $n + \frac{1}{2}$ of real argument, and circular and hyperbolic functions. For example, using the theory of Bessel functions,[14] and after some manipulation of the Mie expressions as given by van de Hulst,† we have

$$a_n = \frac{\left[\frac{A_n}{m} + \frac{n}{x}\right] J_{n+\frac{1}{2}}(x) - J_{n-\frac{1}{2}}(x)}{\left[\frac{A_n}{m} + \frac{n}{x}\right] [J_{n+\frac{1}{2}}(x) + i(-)^n J_{-n-\frac{1}{2}}(x)] - J_{n-\frac{1}{2}}(x) + i(-)^n J_{-n+\frac{1}{2}}(x)}, \tag{5}$$

where A_n involves the Bessel functions with complex argument mx and may be reduced to the form

$$A_n(mx) = -\frac{n}{mx} + \frac{J_{n-\frac{1}{2}}(mx)}{J_{n+\frac{1}{2}}(mx)}.$$

The expression for b_n is exactly as in (5) except that A_n/m is replaced by mA_n wherever it occurs.

†See p. 123 of Ref. 1.

Actually the expression for $A_n(mx)$ takes on the following very simple recursion form:

$$A_n(mx) = -\frac{n}{mx} + \frac{1}{\frac{n}{mx} - A_{n-1}(mx)}, \tag{6}$$

and it can be evaluated for any positive integer n from the formula

$$A_0(mx) = \frac{J_{-1/2}(mx)}{J_{+1/2}(mx)} = \operatorname{ctn}(mx).$$

From formula (6) it is clear that A_n is real when m is real, and (5) reduces to the corresponding expression for dielectric spheres.

The half-order Bessel functions of argument x can also be generated with the usual recursion formulas,[14] and the problem of determining the real and imaginary parts of any A_n is one of rationalization and algebra. The coefficient b_n may be treated similarly. Further, the angular functions π_n and τ_n reduce to Legendre polynomials and their first and second derivatives, which again are amenable to recursion techniques and well adapted to digital computers. (See Appendix A for details.)

The above calculations were programmed for the IBM-704 calculator at RAND in the FORTRAN language. The program has now been adapted for the IBM-7090. All the necessary functions were generated by the corresponding recursion formulas. The quantities a_n and b_n were terminated either when

$$\frac{|a_n|^2 + |b_n|^2}{n} < 10^{-14}, \qquad \text{or when } n = 1.2x + 9.$$

The latter criterion is somewhat more stringent than that used by Penndorf and Goldberg,[15] who have published detailed tables pertaining to the coefficients for dielectric spheres. The values from the IBM-704 checked exactly with the tables cited above in the case where an identical index of refraction was used. Thus, an accuracy of at least five decimal places was achieved in the functions a_n, b_n, $x^{-2}S$, $x^{-4}i$, K_{ext}, and K_{sc}.

In the choice of refractive index, we were guided by indices summarized by Centeno[16] for liquid water in the visible and infrared regions, and by van de Hulst[1] for iron spheres in the visible. The actual indices used initially are listed in Appendix B. The size interval and size range, as well as the interval in the scattering angle θ, were varied to obtain a good description without either too much or too little detail in the numerical results. The choice here is also governed by the numerical integration with respect to particle size eventually required to obtain the resultant parameters for a sample distribution in a polydispersed medium.

As for computing time, one of the longest runs on the IBM-704, involving x in 50(0.5)70 and θ in 0°(0.5)5(1)10(5)180°, took less than thirty minutes. (Note that for $x = 70$ about 100 terms in the series appearing in expressions (1) to (4) have to be evaluated before convergence is achieved.)

Once the primary quantities (1), (2), (3), (4) are known, the following derived quantities may easily be determined:

$$i_1(x, m, \theta) = |S_1|^2 = S_1 S_1^*, \tag{7}$$

$$i_2(x, m, \theta) = |S_2|^2 = S_2 S_2^*, \tag{8}$$

$$i_3(x, m, \theta) = \mathrm{Re}\{S_1 S_2^*\}, \tag{9}$$

$$i_4(x, m, \theta) = -\mathrm{Im}\{S_1 S_2^*\}, \tag{10}$$

where the asterisk denotes the complex conjugate of the quantity; and

$$K_{abs}(x, m) = K_{ext} - K_{sc}. \tag{11}$$

Here i_1 and i_2 are proportional to the intensities of the light scattered per unit solid angle into the direction θ with respect to the direction of the incident light, which consists of two units of parallel flux of neutral radiation; these quantities give the degree of linear polarization; i_3 and i_4 are related to the Stokes parameters that describe the plane of polarization and the ellipticity; and K_{abs} is the relative absorption cross section in the case of absorbing particles.

All the functions (1) to (4) and (7) to (11) were printed out on standard IBM sheets for the various indices of refraction and ranges of parameters shown in Appendix B. For obvious reasons, it is not possible to present here a complete table of values. In the following sections, we shall attempt to describe various features of the results by means of selected examples. For the substance and wavelength corresponding to these examples, the reader is referred to Appendix B.

RESULTS

THE COEFFICIENTS a_n AND b_n

AS VAN DE HULST has shown,† the coefficients a_n and b_n, when plotted in the complex plane, always fall on a circle of radius 0.5 with the center at (0.5, 0.0) provided m is real. He also pointed out that this is no longer true when m is complex and the absorption is large. The present computations give a more detailed description of the Mie coefficients for partially absorbing spheres.

Figures 1*a* and 1*b* show the continuous variation of $a_1(x)$ and $b_1(x)$ as a function of x in the complex plane for nonabsorbing and for slightly absorbing spheres. In the nonabsorbing case, both coefficients trace the circle clockwise. When a small amount of absorption is introduced, the curves begin to spiral inward from the circle, and a series of small, counterclockwise loops appear, which increase in size and show a tendency to converge toward an area near the center of the circle.

An increase in absorption index from 0.0472 to 0.0645 (Fig. 1*b*) has the effect of amplifying the loops and "accelerating" the convergence toward an area near the center of the circle. In both cases $b_1(x)$ develops its loops for smaller x than $a_1(x)$; otherwise its behavior in the complex plane is quite similar to $a_1(x)$. The higher order coefficients also show a similar behavior when plotted in this way.

The case of very large absorption (metallic spheres) has been adequately described by van de Hulst.‡ Our comparable results (not shown in a separate diagram) corroborate the fact that $a_1(x)$ traces a single loop, and thereafter its locus rapidly approaches a counterclockwise circle as x increases. In the case of $b_1(x)$, the same limiting circle appears, centered at (0.5, 0.0) and with a radius equal to one half the absolute value of the Fresnel reflection coefficient for perpendicular incidence.

$$|R| = \left|\frac{m-1}{m+1}\right| = \left[\frac{(r-1)^2 + r'^2}{(r+1)^2 + r'^2}\right]^{1/2}. \tag{12}$$

†See pp. 135, 276*ff*. of Ref. 1.
‡See p. 276, Fig. 55, and p. 279 of Ref. 1.

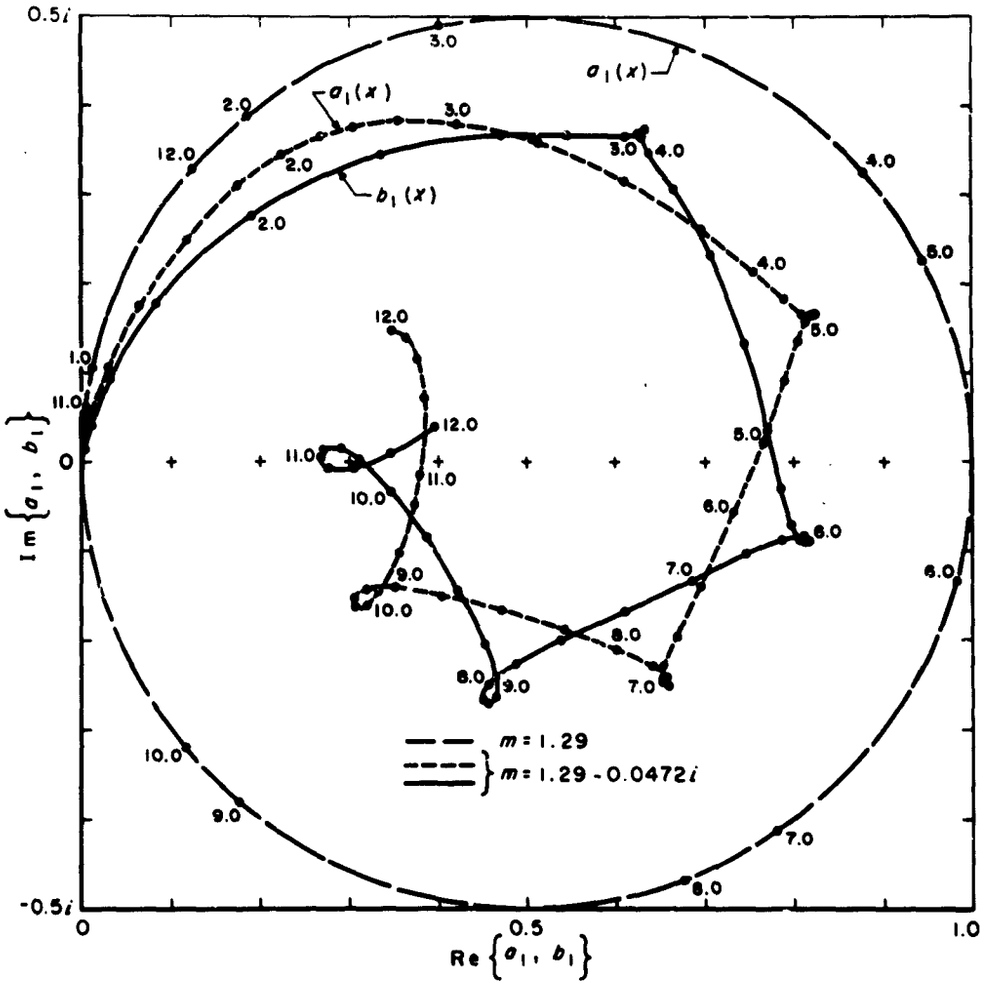

FIG. 1—The effect of absorption on the complex coefficients $a_1(x)$ and $b_1(x)$, the first terms in the Mie series. Computed points are represented by dots and corresponding x-values are shown along the curves. (*a*) $m = 1.29 - 0.0472i$ in the range $x = 0(0.25)12.0$. The outer circle corresponds to $a_1(x)$ for $m = 1.29$ (no absorption). (*b*) $m = 1.29 - 0.0645i$ in the range $x = 0(0.5)18.0$. The outer circle corresponds to $b_1(x)$ for $m = 1.29$.

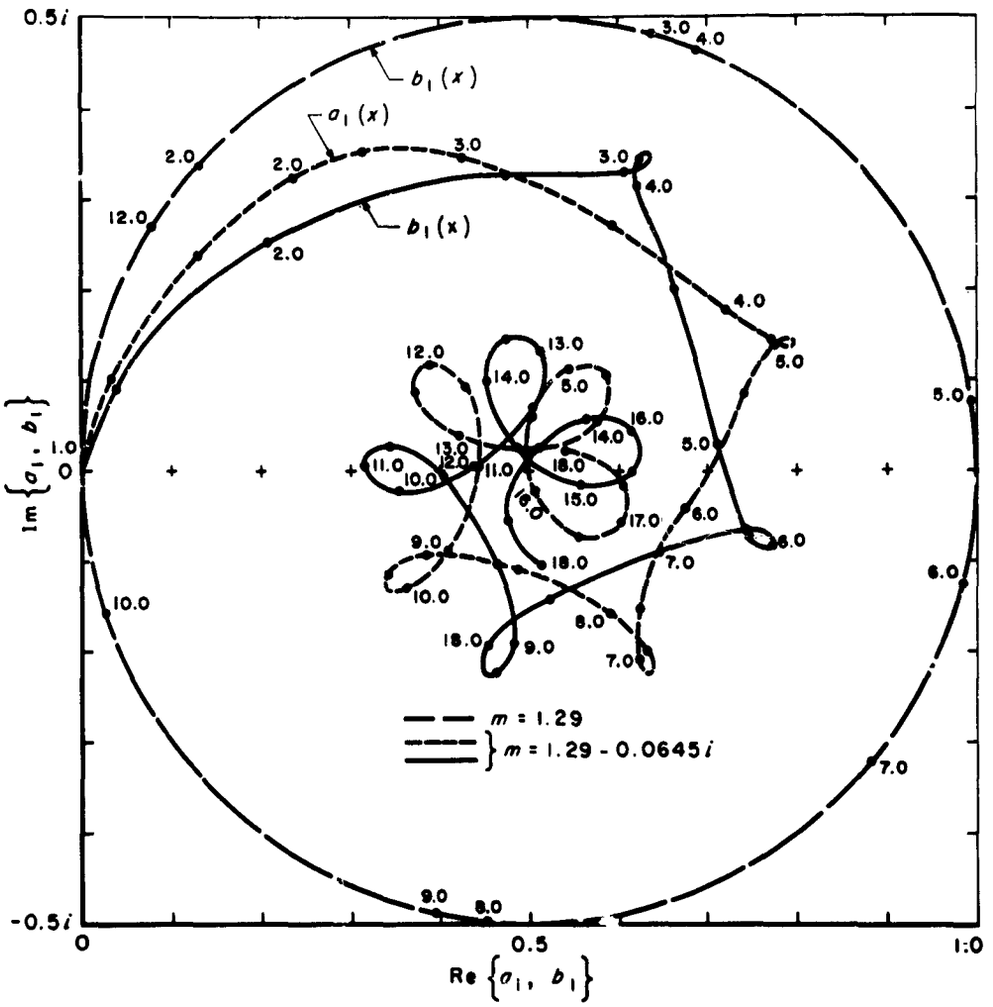

(b)

FIG. 1—*continued*

From the foregoing, it may be presumed that, for small and moderate absorption and for sufficiently large values of x, the loops will also degenerate into a circle with diameter given by (12).

Note in Fig. 1 that for a given x the points $a_1(x)$ and $b_1(x)$ for $m = r$, and $m = r - ir'$ fall on the same radius drawn from the center of the circle. This indicates that the absorp-

tion reduces the magnitude of both $|a_n - \frac{1}{2}|$ and $|b_n - \frac{1}{2}|$ by a factor that increases with r'/r and with x, *provided* r'/r *is small*. The damping effect of the absorption index r' on a_n and b_n does not apply for all x, however. For sufficiently small x, the addition of absorption results in higher values of these coefficients, particularly b_n.

Another way of plotting these coefficients is to keep x constant and vary n. This kind of representation (not shown in a separate diagram) again shows the damping effect described above, the effect increasing with r/r' but not necessarily with n. As n increases, the values of a_n and b_n always tend to zero for some n that depends on x, indicating the point of convergence of the series in expressions (1) to (4). In general, interpolations of individual values of these coefficients, either with respect to x and n, or r and r', should not be necessary once a correct computing program has been worked out. Interpolations of the functions involving the summed series may be necessary and are justified by the smoothness of these functions.

THE AMPLITUDE AND INTENSITY IN THE FORWARD DIRECTION

Figure 2 represents a smooth curve in the complex plane fitted to the computed values of $x^{-2}S(0°)$ as a function of x, where $S(0°)$ is the amplitude of the wave scattered in the forward direction ($\theta = 0°$) for absorbing and nonabsorbing spheres, respectively. In this direction, the polarization of the incident light is preserved for all complex indices of refraction. The case $m = 1.29$ may be compared directly with that for $m = 1.33$ shown by van de Hulst.† In Fig. 2 the values extend to $x = 22.5$ with intervals of 0.25 in x. Loops appear for $x > 8$ increasing in frequency with x. For $x \to \infty$, these should degenerate into the point $(\frac{1}{2}, 0)$, which is the geometric-optics (or high-frequency) limit given by the diffraction term.[11]

The curve for $m = 1.29 - 0.0645i$ shows that the addition of absorption in general damps the amplitude, that the loops appear at larger values of x, and that the diffraction limit is reached for smaller values of x than in the case of pure dielectric spheres. The smoothness of this spiral indicates that it is possible to extend the analytical approximations of van de Hulst‡ for $|m - 1| \to 0$ to include absorbing spheres. When $|m - 1|$ is finite, the van de Hulst expressions may be considerably improved by means of a correction term.[3] However, this possibility is limited only to the forward amplitude and the total extinction cross section (see the following section).

†See p. 264 of Ref. 1.
‡See p. 176 of Ref. 1.

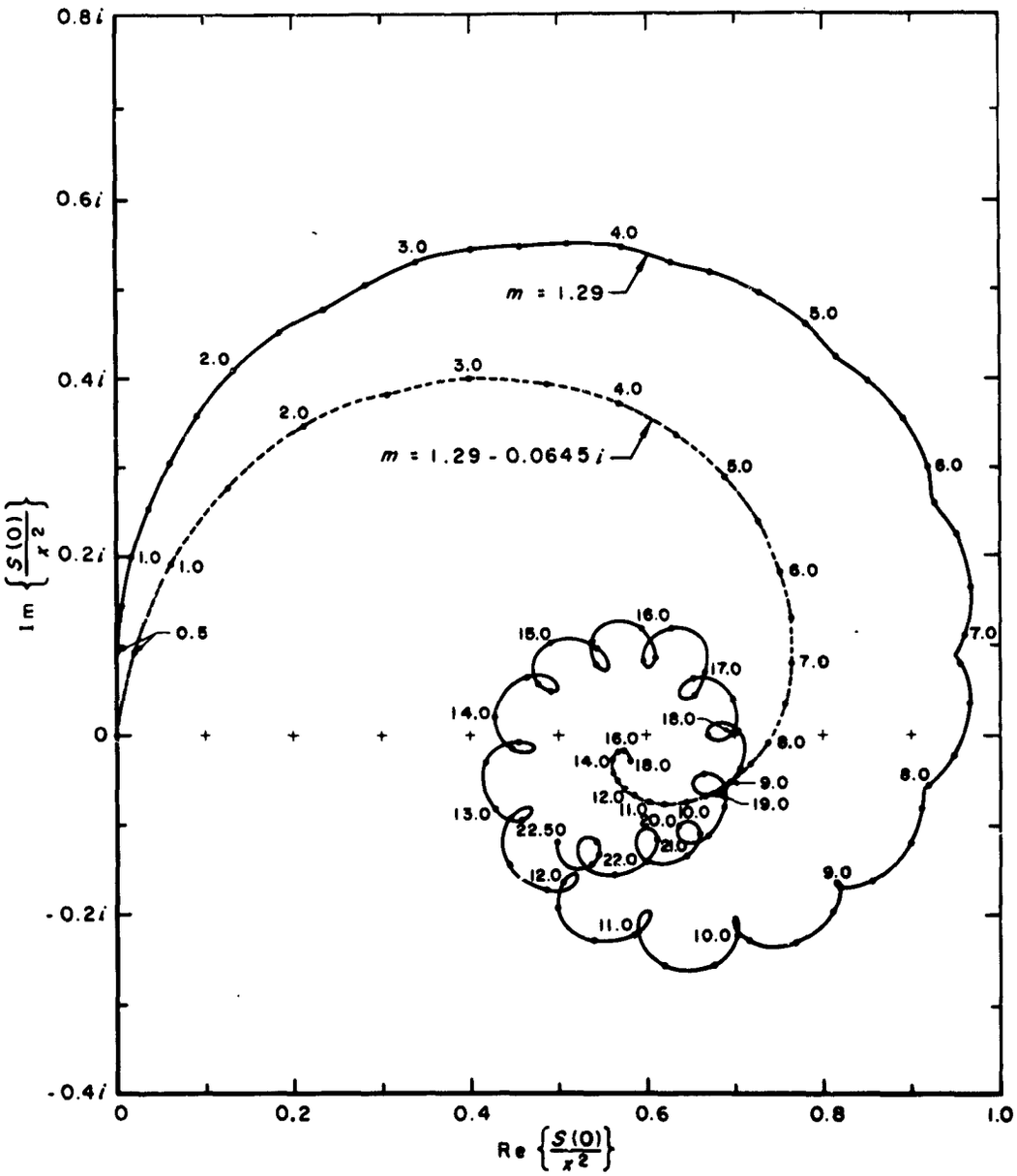

FIG. 2—Continuous variation in the complex plane of the amplitude function in the forward direction, $x^{-2}S(0°)$, as a function of x for $m = 1.29$ (full line) and $m = 1.29 - 0.0645i$ (dashed line). Dots and numbers refer to x-values in the range 0(0.25)22.5 and 0(0.5)18, respectively.

The effect of increasing the real part r of the index of refraction, but keeping r' constant, is to introduce waves and loops in the smooth spiral. The geometric-optics limit is approached more slowly than in the case of r near unity. However, this limit has always the value ½ regardless of the optical properties of the sphere.

Figure 3 is a plot of the quantity $x^{-1}i(0°)$ equivalent to the square of the absolute value of the amplitude shown in Fig. 2. This quantity is proportional to the theoretical intensity of the light scattered exactly in the forward direction, which, of course, cannot be distinguished from the transmitted light experimentally. The damping effect of the absorption on both the large- and small-scale oscillations is clearly seen by comparing the curves for $m = 1.29$ (full line) and $m = 1.29 - 0.0645i$ (dashed line). Increasing the real part of m (dash–dot curve) is equivalent to shifting the first resonance maximum toward smaller sizes.

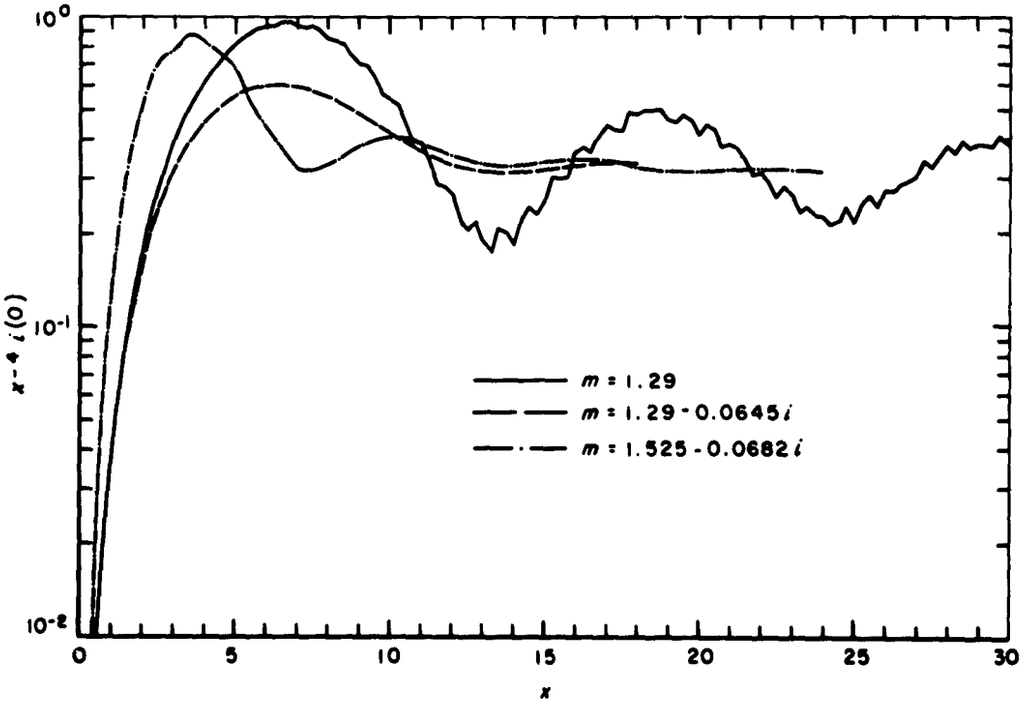

FIG. 3—The logarithm of the intensity function at zero scattering angle, $x^{-1}i(0°)$ as a function of x for the three indices of refraction shown. Points computed at intervals of 0.25 in x have been joined by straight lines. The minor oscillations in the full line curve correspond to the oscillations and loops of the amplitude spiral in Fig. 2.

For sufficiently large x, all curves in this type of representation, regardless of m, approach the straight line $x^{-4}i(0°) = 0.25$, which is the geometric-optics limit.

The curves in Fig. 3 are also related to the infrared aureole near the sun's limb[7][8] produced by atmospheric water droplets (see Appendix B). The scattered intensity for a given droplet size is determined on the curves by the equivalent x value. Furthermore, the area under the curves in Fig. 3 is a measure of the aureole intensity at the sun's limb, assuming a particle concentration that varies as a^{-4}. In the latter case, two conclusions are immediately evident: (1) The aureole intensity at small angles must increase with an increase in the upper limit of particle size. (2) If the range in size would be wide enough, it becomes difficult to distinguish absorbing and nonabsorbing particles by measuring the aureole intensity only at small angles. However, if the particles are relatively small ($x < 10$), and still show the a^{-4} distribution, the aureole intensity next to the limb should be larger for nonabsorbing ($m = 1.29$) than for absorbing ($m = 1.29 - 0.0645i$) particles. On the other hand, if the real part of the index is increased ($m = 1.525 - 0.0682i$), the smaller particles become more efficient scatterers in the forward direction.

THE EXTINCTION AND ABSORPTION CROSS SECTIONS

The extinction cross section is connected to the amplitude of the wave scattered in the forward direction according to the cross-section theorem, which in the present notation takes the form

$$K_{ext}(m, x) = \frac{4}{x^2} \operatorname{Re}\{S(0)\}. \tag{13}$$

Figures 4*a* to 4*c* show examples of the extinction and absorption cross sections plotted as a function of van de Hulst's normalized parameter $z = 2x(r - 1)$. With an appropriate relabeling of the z-axis, the graphs may be made to represent variations of the cross sections with wavelength or with the size of the particles. The three cases shown correspond to refractive indices with identical real parts but increasing imaginary parts representing liquid water droplets illuminated by infrared radiations of different wavelengths (see Appendix B).

The full lines with dots in Figs. 4*a* to 4*c* show the exact Mie values computed according to (3), (4), and (11). It is known from previous analyses[1][18] that in this type of representation the extinction shows a principal maximum around $z = 4$ with a damped periodic shape for larger values of z. With the inclusion of increased amounts of absorption, the principal maximum is damped until it disappears (Fig. 4*c*) and reduces to a plateau. The larger the absorption, the smaller the value of z at which the asymptotic value $K_{ext} \to 2$ as

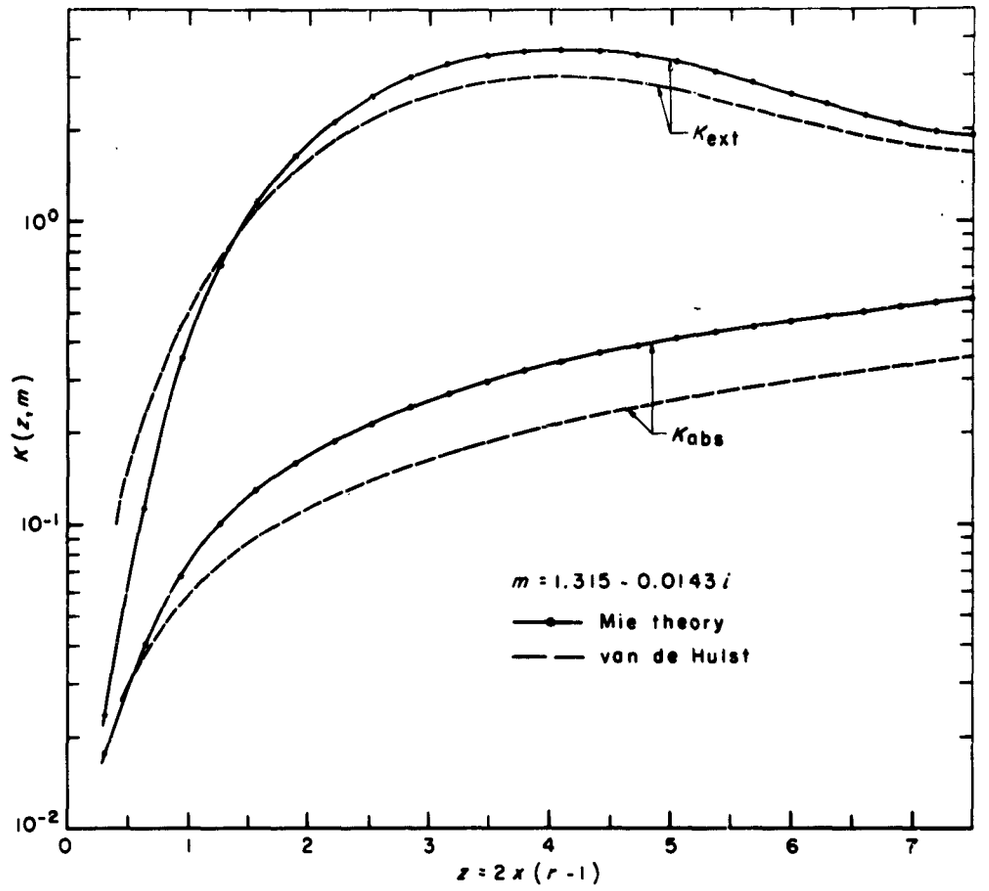

FIG. 4—The logarithm of the extinction and absorption cross sections K_{ext} and K_{abs}, as a function of the normalized size parameter $2x(r-1)$. Full lines with dots indicate exact Mie values. Dashed lines correspond to the equivalent analytical function in van de Hulst's approximation for $|m| \to 1$, computed for the same index of refraction. The three sets of curves refer to a refractive index $r = 1.315$ and an absorption index of $r' = 0.0143$ (a), 0.1370 (b), and 0.4298 (c), respectively.

$z \to \infty$ is reached. Further, as pointed out in the previous section (see also Fig. 2), the secondary oscillations in K_{ext}, characteristic of nonabsorbing spheres, all but disappear when absorption is introduced. In this respect, it should be noted that the extinction curves computed by Johnson and Terrell[2] contain some errors, which must be attributed to an insufficient accuracy in their generating functions. For example, the apparent discontinuity shown

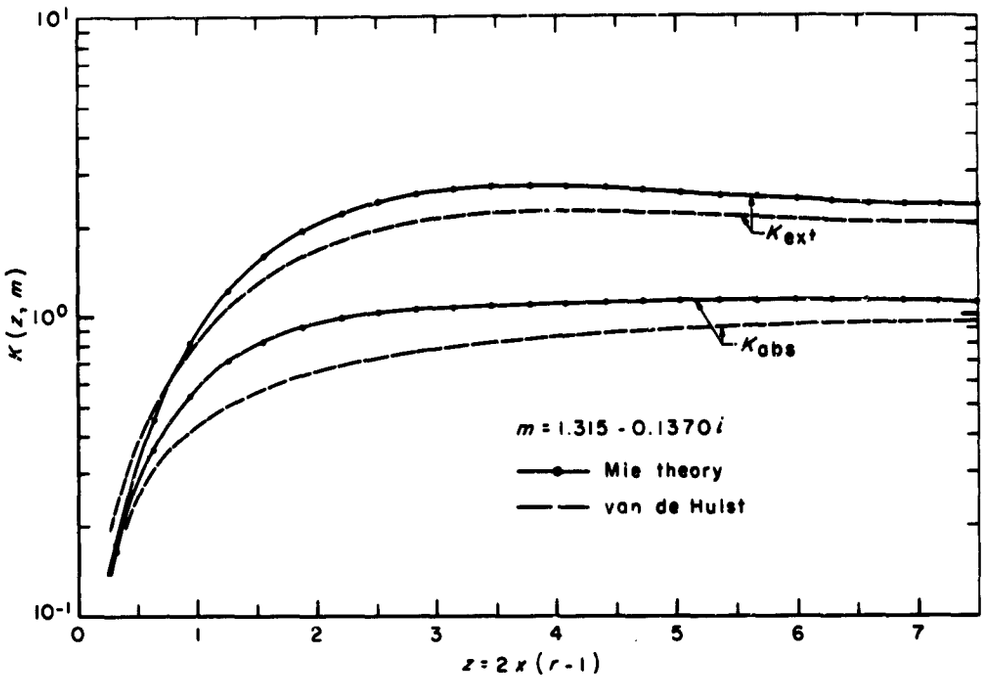

(*b*)

FIG. 4—*continued*

in their curve for $m = 1.29(1 - 0.05i)$ between $x = 6.6$, and $x = 7$ was not reproduced when we repeated this case in our program. Compare the following values of K_{ext} in Table 1. The comparison with our values, which carry an accuracy of five decimal places, shows that one must generate the basic Mie functions to several significant figures to obtain sufficient accuracy in the summations. Except for such details, the values of Johnson and Terrell[2] are essentially correct.

Table 1

K_{ext} for $m = 1.29(1 - 0.05i)$

Source	x						
	1	2	4	6	6.6	7	17
Johnson and Terrell[2]	0.261	0.864	2.28	3.07	3.19	3.06	2.40
The present report	0.2496	0.8563	2.275	3.007	3.062	3.055	2.319

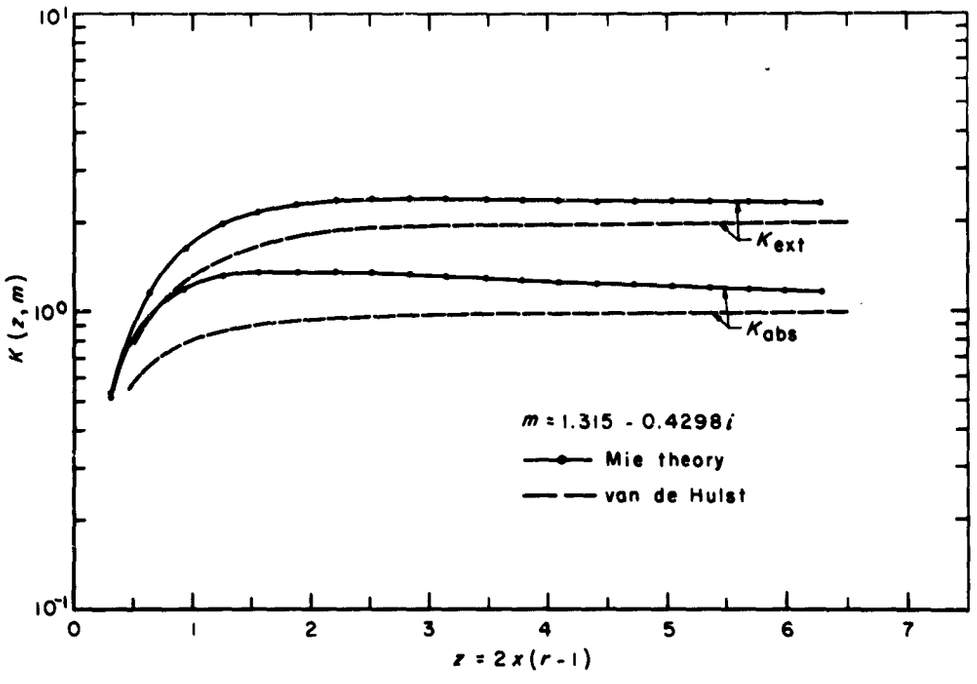

(c)

FIG. 4—*continued*

The dashed curves in Figs. 4*a* to 4*c* show the cross sections computed for the same indices by means of van de Hulst's† analytical approximations without correction.[3] The general shape of the exact curves is reproduced, but there is a systematic deviation especially in the curves for K_{abs}. These deviations in the extinction curves seem to vanish as $z \to \infty$ but not necessarily in the absorption curves. A useful extension of these approximations has been discussed elsewhere,[3] and the correction factors proposed are found to check against the present exact computations of the extinction cross section.

VARIATION OF THE COMPLEX AMPLITUDE WITH SCATTERING ANGLE

The angular dependence of the complex amplitudes $S_1(\theta)$ and $S_2(\theta)$ for any given x and m may be represented by continuous curves on the complex plane. The usefulness of this

†See pp. 179 and 181 of Ref. 1.

representation in interpolations of the amplitude with respect to θ is limited to relatively small sizes, say $x < 8$. For our purposes, it is more interesting to compare the amplitude curves for dielectric and for partially absorbing spheres of an identical size and refractivity, since this has not been done previously.

Figure 5 shows the amplitudes for particles with $x = 1$ for the three indices shown. For real index, the amplitude plots for $S_1(\theta)$ and $S_2(\theta)$ are practically straight lines almost parallel to the imaginary axis. There is very little variation in the magnitude

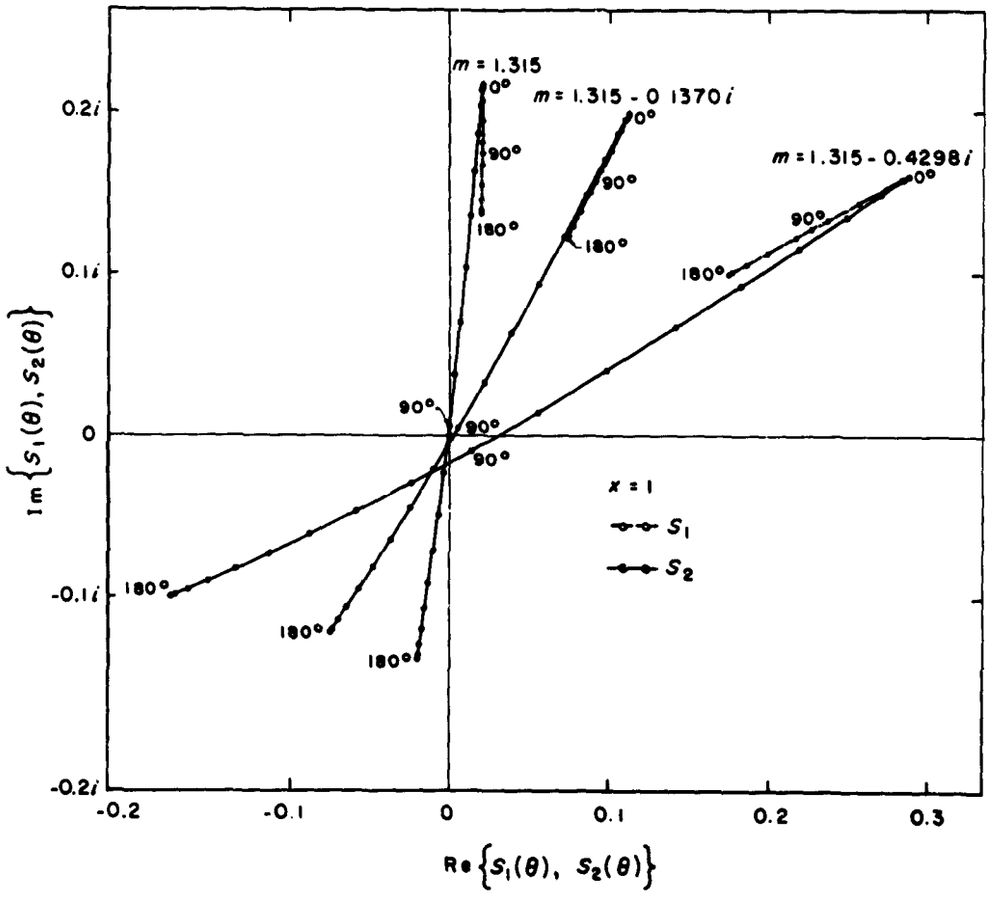

FIG. 5—The effect of increasing absorption on the amplitude functions $S_1(\theta)$ (dashed line) and $S_2(\theta)$ (full line) plotted on the complex plane, in the case of a small sphere ($x = 1$). Dots indicate computed points at 10° and 20° intervals in θ. Those for 0°, 90°, and 180° scattering are labeled. The three curves correspond to $r = 1.315$ and $r' = 0$, 0.1370, and 0.4298, respectively, as indicated.

of $S_1(\theta)$ with θ, but that of $S_2(\theta)$ is minimized near $\theta = 90°$. This feature is similar to that obtained in the Rayleigh limit, ($x << 1$), where, in the first approximation, we have $S_1(\theta) = ix^3(m^2 - 1)/(m^2 + 2)$ and $S_2(\theta) = ix^3 \cos\theta\,(m^2 - 1)/(m^2 + 2)$, respectively. The other curves on Fig. 5 show that the amplitude at all angles *increases* with the absorption index, mainly because of a larger real part. Further, all three cases are represented by almost straight lines, with the trivial conclusion that interpolation with θ becomes very easy when x is small. For any $x < 1$, the expansion of the amplitude in power series of x, mentioned by van de Hulst,† and used by Penndorf[11] in calculating the cross sections, may be adequate for the amplitudes as well.

For greater values of the size parameter x, the amplitudes show large fluctuations with θ, particularly in the backward hemisphere. This creates a problem in the choice of an interval $\Delta\theta$ small enough to obtain all the details of the angular scattering pattern. To illustrate this point, we plotted the amplitudes corresponding to $x = 4$, on the same basis as in Fig. 5. Figure 6*a* corresponds to $m = 1.315$ and may be compared with a similar case shown by van de Hulst.‡ The characteristic large amplitudes at small scattering angles, where $S_1 = S_2$, and the rapid decrease in amplitude with increasing θ are clearly evident. For this relative size, a computation with $\Delta\theta = 10°$ is necessary for a graphical interpolation of the amplitude with respect to θ. Figure 6*b*, for $m = 1.315 - 0.1370i$, shows that the effect of absorption in this case is to *decrease* the magnitude of the amplitude considerably at all angles, contrary to the effect shown on Fig. 5. Note also the reversal of the looping in $S_2(\theta)$ near 180°, as compared with Fig. 6*a*. At 180°, of course, we always have $S_2(180°) = -S_1(180°)$. Increasing the absorption still further (Fig. 6*c*) results in still smaller amplitudes, which, near the forward direction, have much smaller imaginary parts. Note again the peculiar looping near the backward directions.

A general feature appearing in Fig. 5 and Figs. 6*a* to 6*c* is that the radius vector from the origin to the forward scatterpoint seems to rotate clockwise with increasing absorption index.

The amplitudes for larger particles ($x = 6$) are partly illustrated in Figs. 7*a* and 7*b* (pp. 22–23). These smooth curves have been fitted to points computed with $\Delta\theta = 2°.5$. Larger intervals would not be sufficient to yield the correct behavior of the function by smooth curve fitting, especially in the backward hemisphere. The number of loops has increased, and in the absorbing case, Fig. 7*b*, there seems to be a cusp in $S_2(\theta)$ near $\theta = 90°$. Van de Hulst's remark that one full turn in such curves takes an interval in θ of the order $360°/x$ is roughly corroborated in Fig. 7*a* but not in Fig. 7*b*. Needless to say, the amplitude curves become in-

† See p. 145 of Ref. 1.
‡ See p. 235 of Ref. 1.

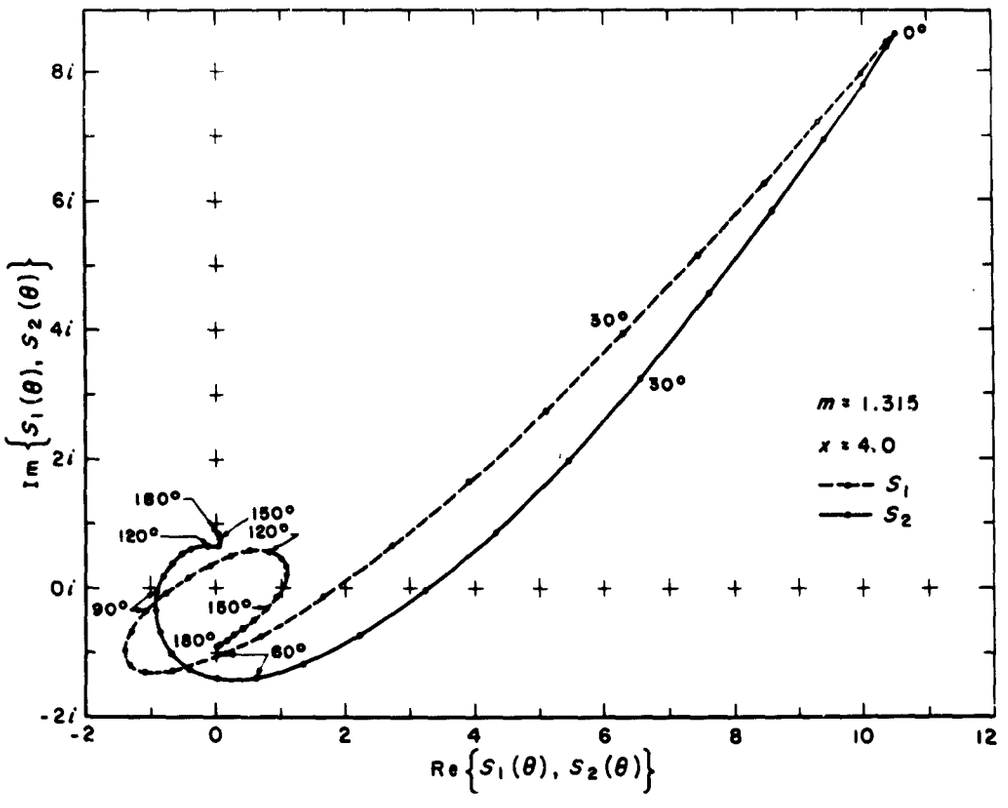

FIG. 6—Representation in the complex plane of the amplitudes S_1 and S_2 for spheres with $x = 4$. The curves for the same indices as in Fig. 5 are shown separately in (*a*), (*b*), and (*c*), covering the full range from 0° to 180° at intervals of 5° in θ.

creasingly complicated for larger values of x, and the intervals in θ must be made even smaller to get an adequate description.

Examples of numerical values of the real and imaginary parts of S_1 and S_2 for a given m and $\theta = 0°$ and 180°, as a function of x, are reproduced in the tables in Appendix C. These show the variability of the amplitude at these angles with changes in the size of the sphere (or changes in the frequency, if the sphere size is constant), for various indices of refraction.

In general, the amplitude curves derived from the exact theory show that it should be relatively easy to replace the Mie series by analytical approximations even in the absorbing case, provided θ is kept small. Otherwise, one should not expect too much from simple in-

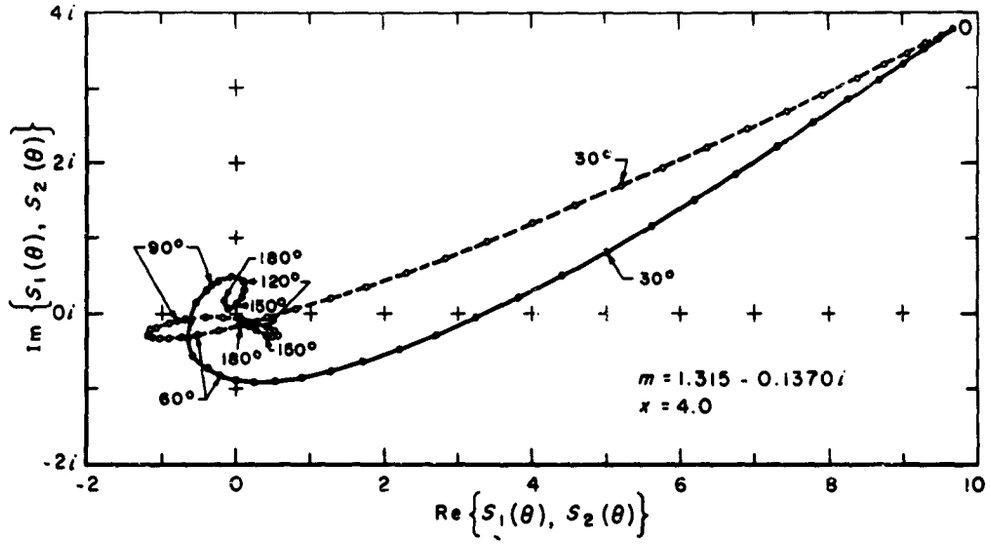

(b)

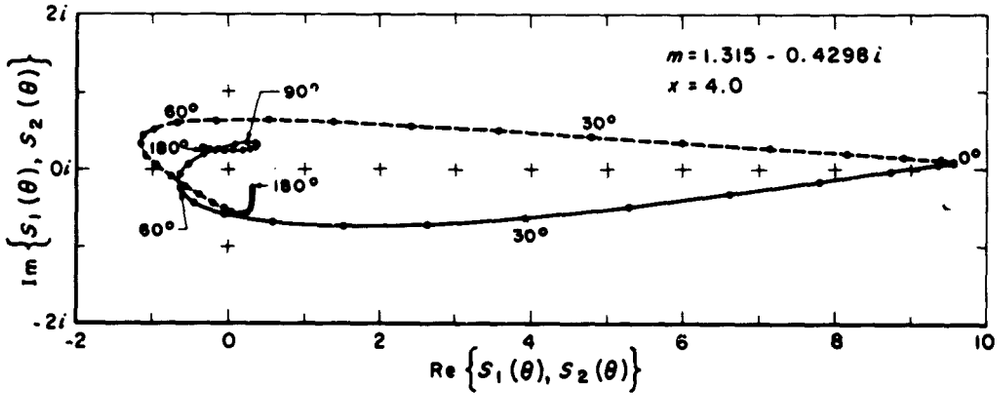

(c)

FIG. 6—*continued*

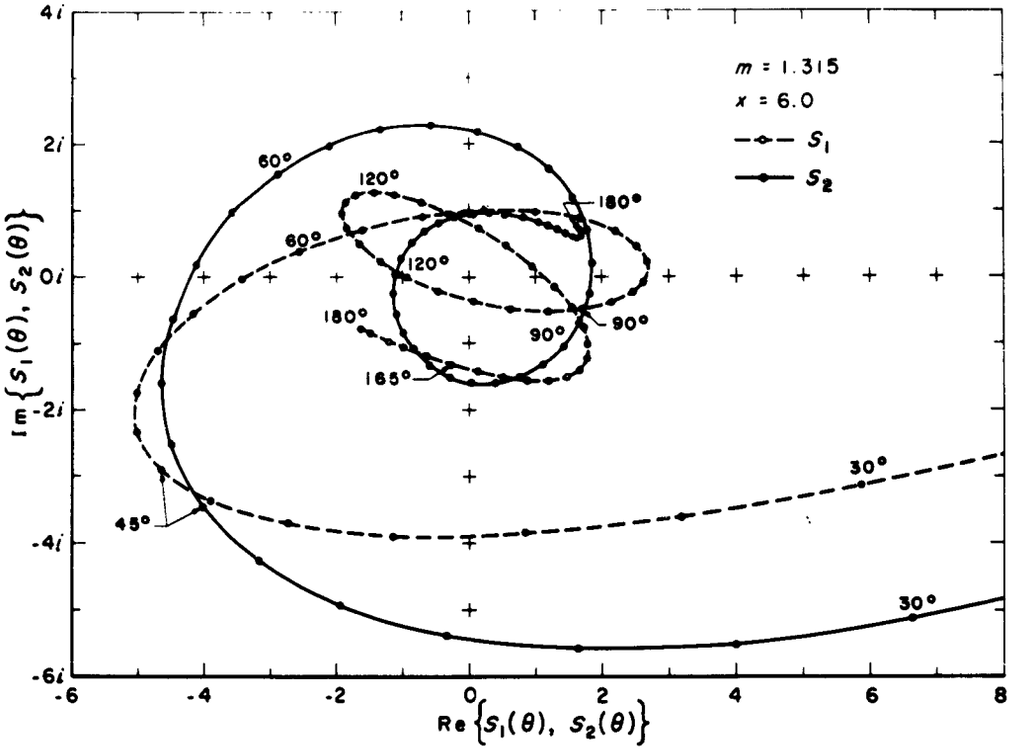

(a)

FIG. 7—The amplitudes S_1 and S_2 for spheres with $x = 6$, computed at intervals of 2°.5 in θ. (*a*) Index of refraction $m = 1.315$, range $30° \leqq \theta \leqq 180°$. The value $S(0°) = 35.566 + 7.3669i$ is not shown as it falls outside the frame. (*b*) Index $m = 1.315 - 0.4298i$, range $22°.5 \leqq \theta \leqq 180°$. The value $S(0°) = 21.459 - 1.4633i$ is not shown.

terior field approximations in the intermediate frequency range. The scattered radiation field depends critically on the interaction of reflected, diffracted, transmitted, and surface waves. One can hardly expect to reproduce these interactions by *ad hoc* separations of the field without reaching a self-defeating degree of complexity in the mathematical expressions.

VARIATION OF THE INTENSITY AND POLARIZATION OF THE SCATTERED LIGHT WITH SCATTERING ANGLE

The normalized intensities defined by (7) through (10) are the most important parameters in problems of radiative transfer for polydispersed media, provided independent or in-

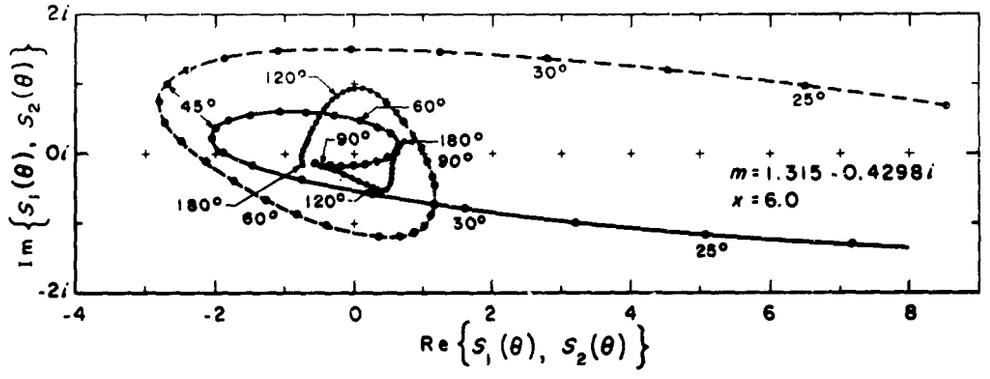

(b)

FIG. 7—*continued*

coherent scattering can be assumed. When the sphere is illuminated by unpolarized radiation, the scattered radiation shows partial linear polarization with the maximum electric field oscillation either perpendicular or parallel to the scattering plane. For convenience, we may define the polarization P in this case by the expression

$$P = \frac{i_1(\theta) - i_2(\theta)}{i_1(\theta) + i_2(\theta)}, \tag{14}$$

so that positive and negative values correspond respectively to the two cases mentioned above. The denominator in (14) always defines the total intensity of the scattered radiation, regardless of its state of polarization.

The remaining parameters $i_3(\theta)$ and $i_4(\theta)$ are related to those elements of the scattering matrix that determine the Stokes parameters defining the plane of polarization and degree of ellipticity of the scattered light when the incident light is polarized.† These parameters are important in problems with multiple scattering even when the incident light is neutral. They will not be discussed here, since one has to specify various types of polarization in the incident light in order to understand their effect in changing the polarization.

Figures 8*a* to 8*c* are logarithmic plots of $i_1(\theta)$ and $i_2(\theta)$ as a function of scattering angle θ, all for $x = 3$ but progressively increasing absorption index. In all three cases it is seen that when the diameter of the sphere is approximately equal to one wavelength, the scattering pattern is highly asymmetrical, and the polarization deviates considerably from

†See pp. 40*ff*. of Ref. 1.

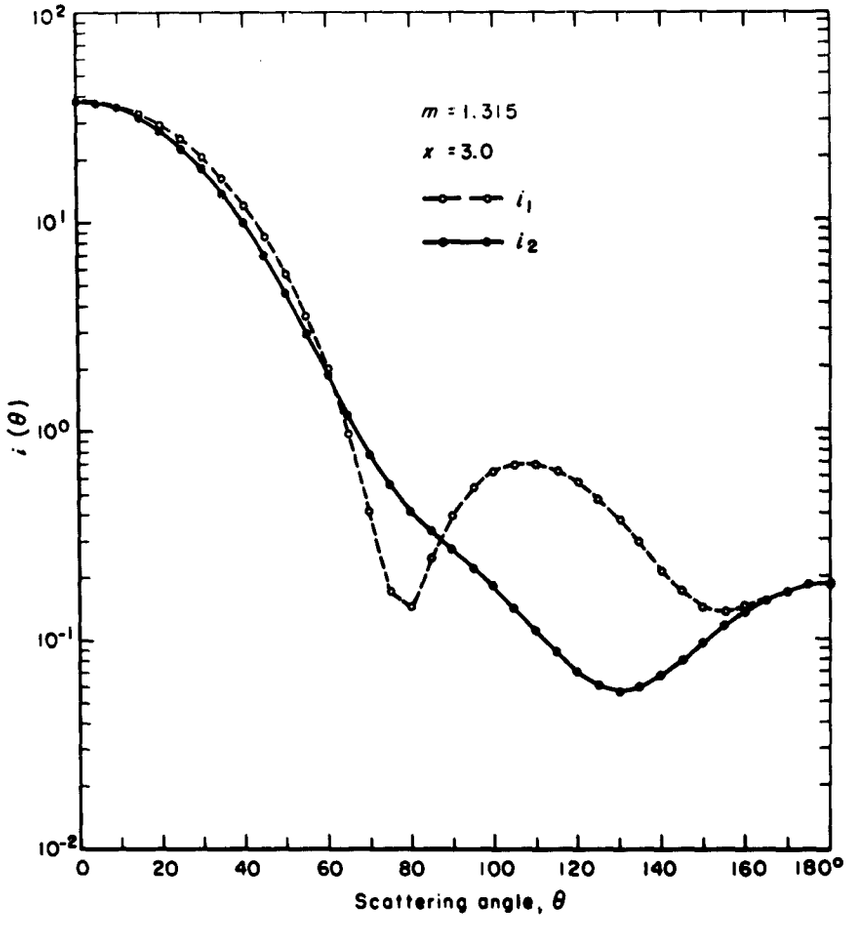

FIG. 8—The logarithm of the intensity functions $i_1(\theta)$ (dashed line) and $i_2(\theta)$ (full line) for spheres with $x = 3$, plotted at intervals of 5° in θ, and joined by straight-line segments. The curves for the three indices $m = 1.315$, $1.315 - 0.1370i$, and $1.315 - 0.4298i$ are shown separately in (a), (b), and (c), respectively.

the Rayleigh case. Light scattered at angles $0° \leq \theta < 40°$ exceeds the back-scattered light at angles $140° < \theta \leq 180°$ by two to four orders of magnitude. It is interesting to note that this ratio does not depend on the absorption properties in a simple manner; for example, the back-scattered intensity for $r' = 0.4298$ (Fig. 8c) is less than that for $r' = 0$ (Fig. 8a), but much larger than that for $r' = 0.1370$ (Fig. 8b). A broad secondary intensity maximum

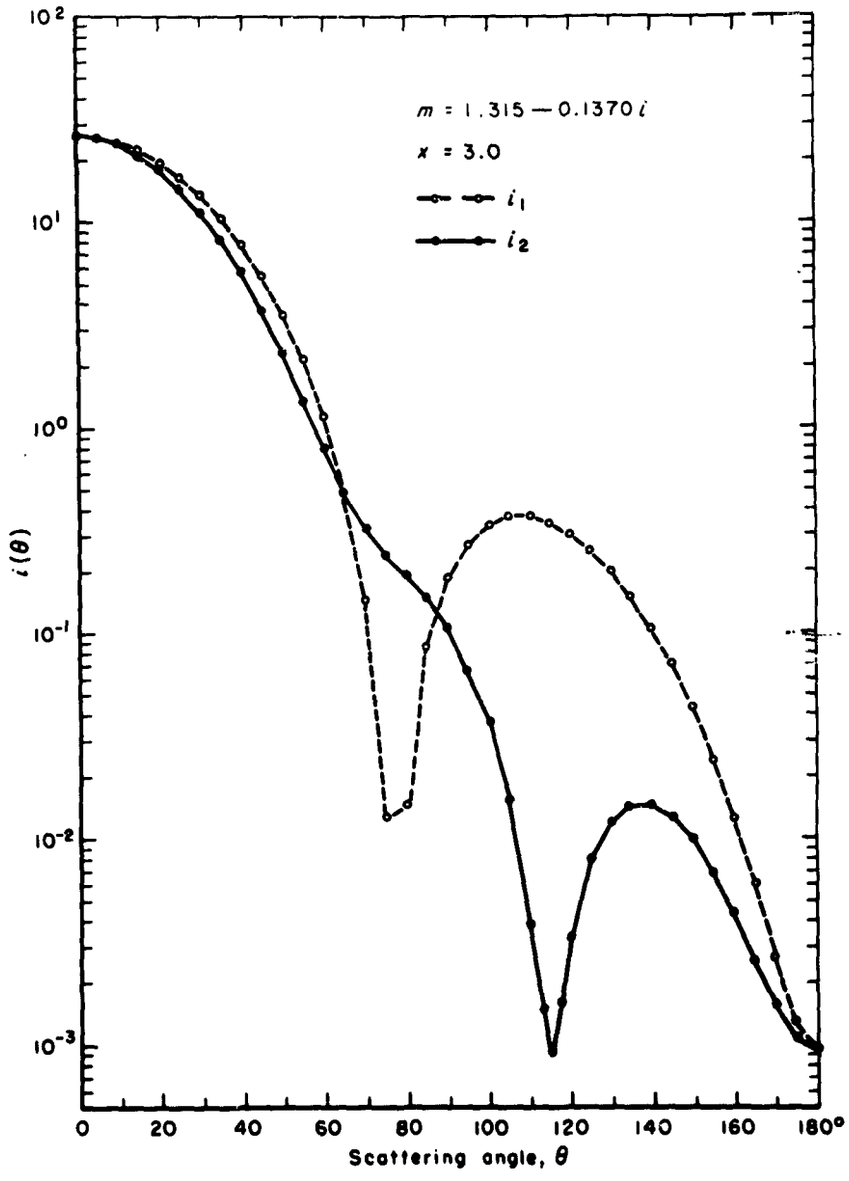

(*b*)

FIG. 8—*continued*

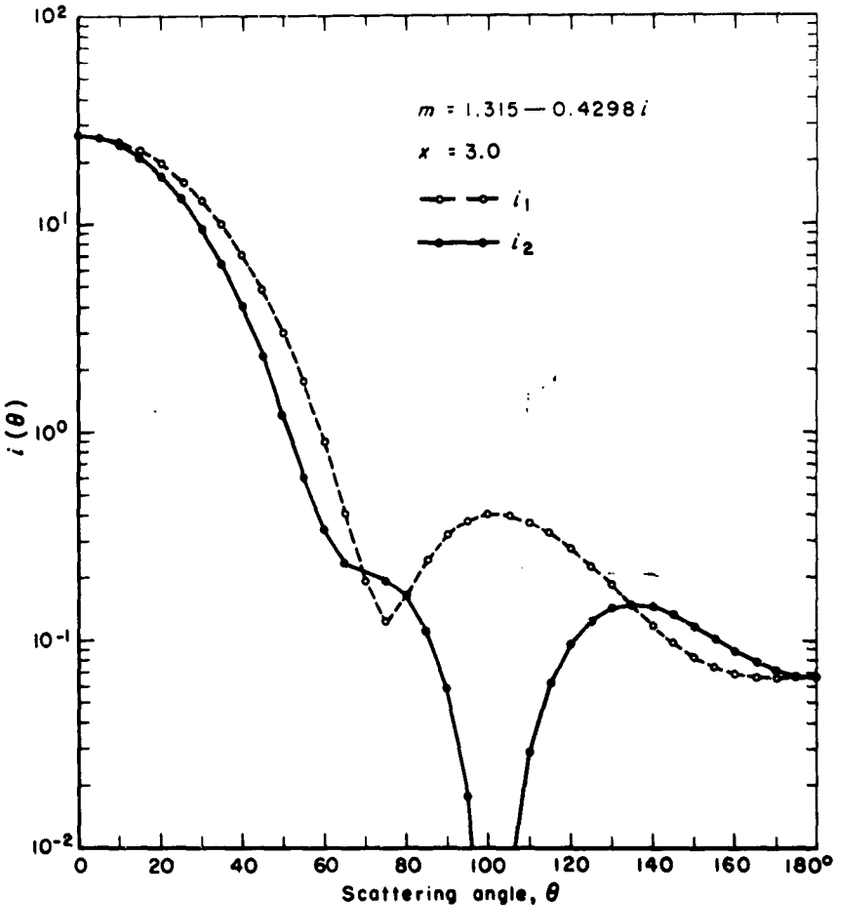

(c)

FIG. 8—*continued*

between 90° and 120° is evident in all cases shown, but it is less pronounced in the most absorbing case.

More interesting are the effects of absorption on the polarization. The sign of polarization for $\theta < 90°$ is the same for all three cases, but in the backward hemisphere it depends on the magnitude of the absorption index. Furthermore, the degree of polarization changes considerably with absorption. In the regions of maximum intensity, especially in the forward hemisphere, the polarization seems to increase directly with absorption, as shown in Table 2.

Table 2

P for $x = 3$, $r = 1.315$

	r'			
θ	0	0.0143	0.137	0.4298
40°	0.098	0.105	0.159	0.281
60°	0.041	0.053	0.166	0.460
100°	0.563	0.593	0.803	0.995

The situation for larger spheres corresponding to $x = 10$ is shown in Figs. 9*a* and 9*b*. The case with a pure dielectric, $m = 1.29$, in Fig. 9*a*, shows a number of secondary maxima as already indicated by the detailed work of Penndorf and Goldberg[18] and reproduced in Ref. 7. Note that the polarization is very weak and negative in the diffraction maximum at $0° < \theta \leq 15°$, and that it changes sign several times at other angles. When a large absorp-

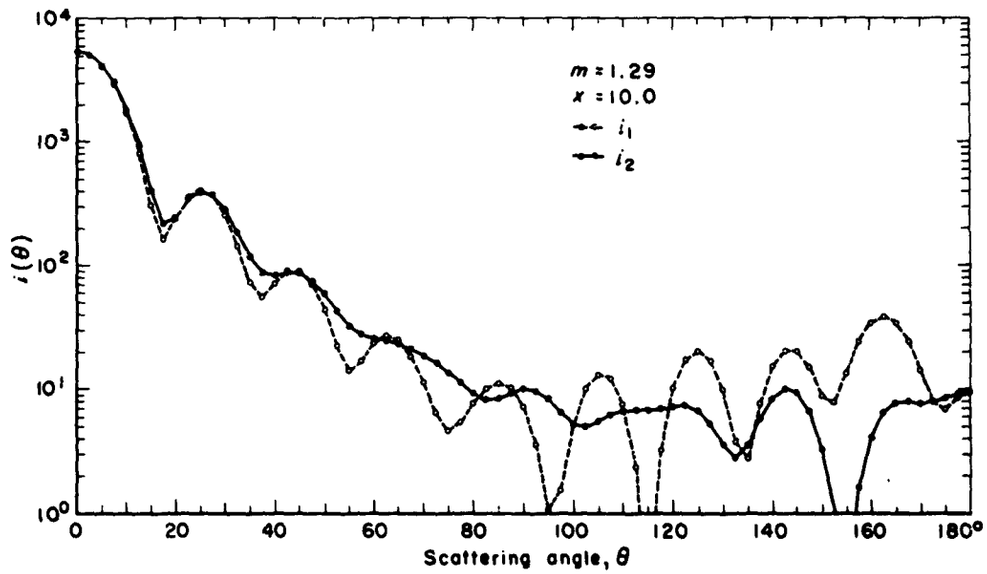

FIG. 9—The logarithm of the intensities i_1 (dashed line) and i_2 (full line) for spheres with $x = 10$, plotted at intervals of 2°.5 in θ. The curves for $m = 1.29$ and $1.29 - 0.4720i$ are shown separately in (*a*) and (*b*), respectively.

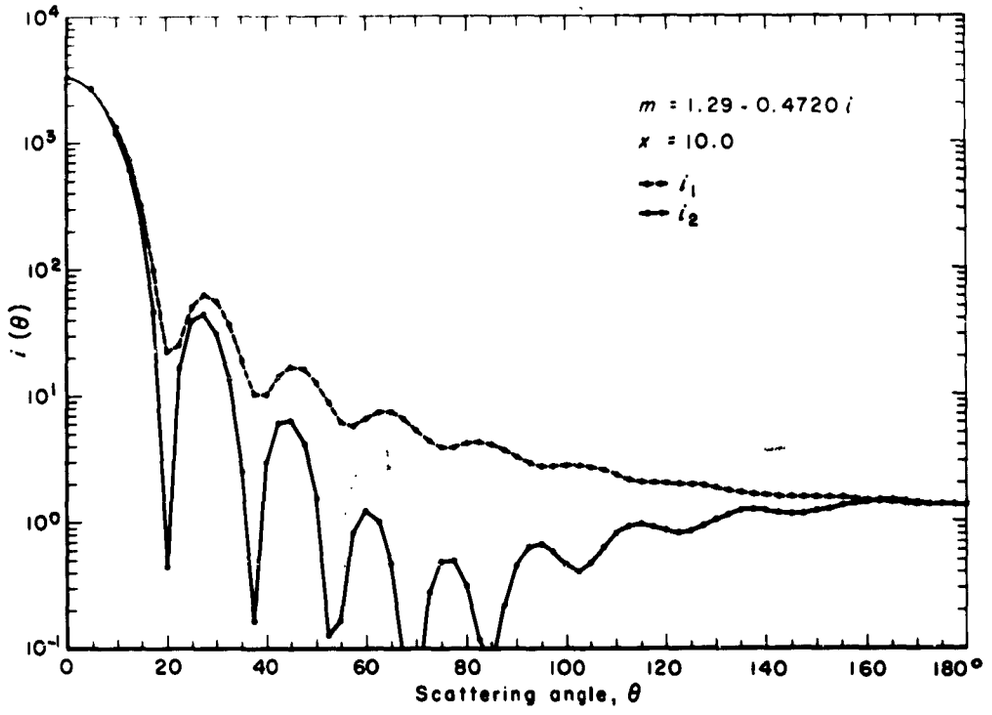

(*b*)

FIG. 9—*continued*

tion is introduced as in Fig. 9*b*, the forward intensity peak remains the same; however, its polarization becomes positive. Furthermore, the polarization in this case remains positive at all angles up to 160°. The scattered intensity field for $120° < \theta \leq 180°$ is very flat compared with the dielectric case, because of the suppression of the components arising from multiple internal reflections.

As mentioned before, with the addition of absorption, polarization in the forward hemisphere increases in the positive direction. This effect becomes more pronounced with increasing size and is most noticeable in the regions of maximum intensity. Compare the polarization values in Table 3 with those given for $x = 3$, with reference to the scattering diagrams in Figs. 8*a*, 8*b*, 8*c*, 9*a*, and 9*b*. In the region 40° to 60° and for $x = 3$, the polarization in the most absorbing case is 3 to 10 times that of a dielectric, while in the same region but for $x = 10$ the increase in polarization is by a factor of 18 to 25.

Table 3
P for $x = 10$, $r = 1.29$

	r'		
θ	0	0.0472	0.4720
25°	0.023	0.031	0.122
45°	0.018	0.089	0.457
62°.5	0.042	0.170	0.762
85°	0.137	0.382	0.964
105°	0.409	0.625	0.701

A physical explanation of this in terms of ray optics may be postulated as follows: As mentioned above, the intensity and polarization of the scattered light is the sum of several streams of light emerging in a given direction. The Fresnel reflection coefficients for the intensities of the two polarized components i_1 and i_2, respectively, after one reflection, may be written in the form

$$|R_1|^2 = \frac{(q-r)^2 + r'^2}{(q+r)^2 + r'^2}, \tag{15}$$

$$|R_2|^2 = \frac{(qr-1)^2 + (qr')^2}{(qr+1)^2 + (qr')^2}, \tag{16}$$

where $q = \sin\tau/\sin\tau'$, and τ and τ' are the inclination angles of the incident and refracted rays, respectively. (Both of these expressions reduce to (12) when $q = 1$; that is, at normal incidence.) Keeping q constant, the examples in Table 4 demonstrate the changes in $|R_1|^2$, $|R_2|^2$, and P with absorption, obtained from (15) and (16). These values show that in general external reflection of the unpolarized incident stream should add positive polarization, so to speak, to the scattered field. This effect should be more pronounced at the smaller angles of scattering where the magnitude of the reflection coefficient is large. The example

Table 4
P from external reflection for $r = 1.29$

	$q = 0.5 (\theta \simeq 40°)$			$q = 0.8 (\theta \simeq 80°)$		
r'	$\|R_1\|^2$	$\|R_2\|^2$	P	$\|R_1\|^2$	$\|R_2\|^2$	P
0	0.192	0.047	0.61	0.055	0.00025	0.99
0.472	0.247	0.066	0.58	0.101	0.034	0.50

further shows that at $\theta \simeq 40°$, the externally reflected rays, in both the nonabsorbing and the absorbing cases, should be positively polarized in the same amount (0.61 and 0.58, respectively). However, the actual polarizations of the scattered light at the same angle (see Figs. 9*a* and 9*b*) are −0.07 for the nonabsorbing and 0.53 for the absorbing case. The negative polarization in the nonabsorbing case may be thought of as the resultant of externally reflected rays plus those transmitted and reflected internally into the same direction. When the latter are suppressed by absorption, the positive polarization of the externally reflected ray dominates the scattered field. In the present example, $r' = 0.472$ corresponds to an exponential absorption coefficient γ, given by

$$\gamma = \frac{4\pi r'}{\lambda} = \frac{5.89}{\lambda}.$$

For example, in visible light, "rays" penetrating the sphere are practically extinguished along a path of a micron or so in the interior of the medium because of the large value of the coefficient γ. This line of reasoning also explains why the effect of absorption on the polarization is not so noticeable in the case of smaller spheres, where interior paths are short and geometric optics does not apply.

Finally, Fig. 10 illustrates some of these points more clearly in the case of metallic spheres. The total intensity, $i_1 + i_2$, and the polarization P are shown separately for an iron sphere illuminated by λ 5890 A radiation ($m = 1.51 - 1.63i$) and a dielectric sphere with $m = 1.525$, both having a diameter of about 2.2 wavelengths. The six secondary maxima in intensity observed in the dielectric case are completely suppressed in the case of an iron sphere. The polarization curves in the inset of Fig. 10 show several maxima and minima in both cases; however, the iron sphere scatters positively polarized light in all directions, whereas the dielectric sphere displays mostly negative polarizations. These differences, particularly in the polarization, are extremely important, for example, in the investigation of the nature of interplanetary particles responsible for the zodiacal light.

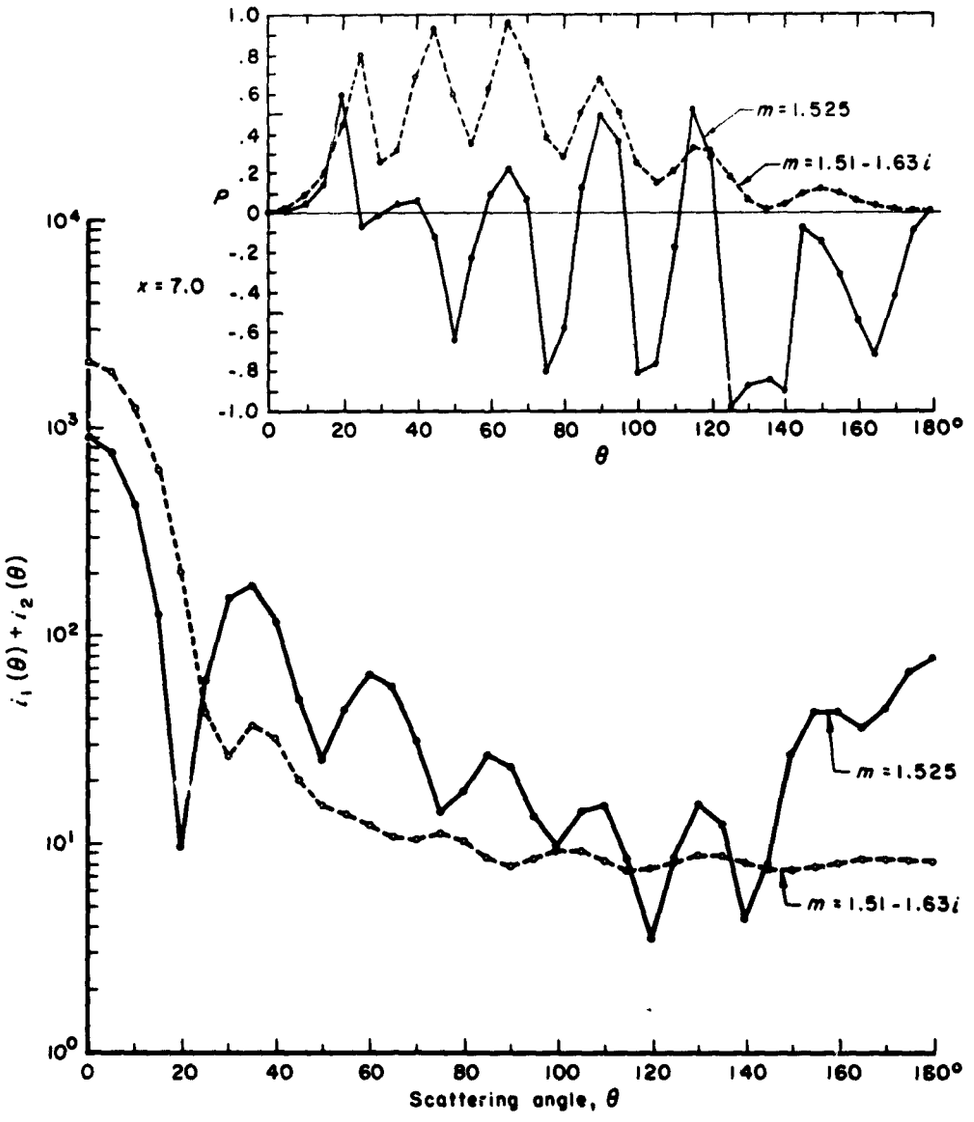

FIG. 10—The logarithm of the total intensity $i_1 + i_2$ for spheres with $x = 7$, plotted at intervals of 5° in θ. The curves for an iron sphere ($m = 1.51 - 1.63i$) and a dielectric sphere ($m = 1.525$) are shown on the same diagram for comparison. The inset shows the degree and sign of partial linear polarization of the light scattered by each sphere in various directions when illuminated by unpolarized light.

SUMMARY AND COMMENTS

ALL THE FUNCTIONS related to the scattering of electromagnetic waves on homogeneous spheres with a complex index of refraction can be easily computed to a high degree of accuracy by modern machines. Thus, the effects of absorption on the mechanism of scattering, especially in the intermediate frequency range, can be exactly assessed without the use of simplifying assumptions based on physical and geometrical optics. Such approximations have proved successful in the high- and low-frequency cases, but they generally fail in the middle range except under severe limitations on the physical properties of the substance in the sphere. It is hoped that the present results, which are based on the exact theory, besides revealing hitherto unknown details of the scattering process, will provide reliable criteria for checking the range of validity of any extensions of approximate theories into the intermediate range.

But there is a still more important application of this type of study. The intermediate range, especially when the physical properties in the sphere differ considerably from those of the surrounding medium, is precisely the range of interest in a class of problems involving the absorption and the diffuse transmission and reflection of sunlight by planetary atmospheres, including our own. In fact, as is known from the terrestrial atmosphere, the maximum linear size of solid or liquid particles that can remain suspended for appreciable lengths of time is limited to a few tens of wavelengths of visible light. It is further known that a small fraction by mass of such "large" particles mixed in a gas is sufficient to alter radically the character of the transmitted and reflected light. Similar remarks apply to interplanetary and interstellar dust particles. Of course, the assumption of spherical particles may not be correct, but it is useful to understand completely their scattering properties before investigating more complicated shapes.

In any case, a complete quantitative-theoretical understanding of the spectrum, intensity, and polarization of the light diffusely reflected by sunlit planetary atmospheres is essential at this time in order to interpret correctly the observational data obtainable by means of instrumented space probes sent to the vicinity of the nearer planets. In the examples pre-

sented, we have shown that, in addition to changes in the size of the spheres, small changes in the absorption index have large effects on the intensity and polarization of the scattered light, particularly at large angles. In the planetary problem, a consideration of models assuming a number of particles that are identical in size and nature is hardly sufficient. Such a situation cannot exist either in planetary atmospheres or in interplanetary and interstellar space. The ultimate purpose of these calculations is to derive the scattering properties of a small sample volume of space containing a representative distribution in the size and the index of refraction of the particles. The resultant values of the elements of the scattering matrix pertaining to the aggregate will be summations of those pertaining to the individual particles. This summation cannot be accomplished without a knowledge of the scattering properties of individual particles. Both theory and existing measurements show that the scattering properties of a polydispersed medium tend to be smooth functions of the scattering angle. The latter, once determined, can be treated analytically to separate the angular dependence from the size dependence in order to solve the corresponding equation of radiative transfer.

APPENDIX A

COMPUTATIONAL SCHEME

IN THE ACTUAL IBM-704 routine (since adapted to the IBM-7090 system) the following scheme was used:

The coefficients $a_n(m, x)$ and $b_n(m, x)$ were expressed in the form

$$a_n = \frac{\left(\frac{A_n}{m} + \frac{n}{x}\right) \operatorname{Re}\{w_n\} - \operatorname{Re}\{w_{n-1}\}}{\left(\frac{A_n}{m} + \frac{n}{x}\right) w_n - w_{n-1}},$$

$$b_n = \frac{\left(A_n m + \frac{n}{x}\right) \operatorname{Re}\{w_n\} - \operatorname{Re}\{w_{n-1}\}}{\left(A_n m + \frac{n}{x}\right) w_n - w_{n-1}},$$

where the function w_n is connected with the half-order Bessel functions appearing in (5) in the text, and has the explicit recursion form

$$w_n(x) = \frac{2n-1}{x} w_{n-1} - w_{n-2}$$

with

$$w_0 = \sin x + i \cos x,$$
$$w_{-1} = \cos x - i \sin x.$$

The recursion form used for $A_n(m, x)$ has already been indicated in (6) in the text with

$$A_0(mx) = \frac{\sin rx \cos rx + i \sinh r'x \cosh r'x}{\sin^2 rx + \sinh^2 r'x},$$

where $m = r - ir'$.

The recursion formulas used for the angle-dependent functions are as follows:

$$\pi_n(\theta) = \frac{(2n-1)}{n-1}\pi_{n-1}(\theta)\cos\theta - \frac{n}{n-1}\pi_{n-2}(\theta),$$

$$\tau_n(\theta) = \cos\theta\,[\pi_n(\theta) - \pi_{n-2}(\theta)] - (2n-1)\sin^2\theta\,\pi_{n-1}(\theta) + \tau_{n-2}(\theta)$$

with

$$\pi_0(\theta) = 0, \qquad \tau_0(\theta) = 0,$$
$$\pi_1(\theta) = 1, \qquad \tau_1(\theta) = \cos\theta,$$
$$\pi_2(\theta) = 3\cos\theta, \qquad \tau_2(\theta) = 3(\cos^2\theta - \sin^2\theta).$$

The scattering functions were then computed by the summation of the absolutely converging series indicated by the expressions (1) to (4) in the text.

APPENDIX B

RANGE OF COMPUTATIONS

THE VARIOUS INDICES of refraction and size ranges covered by our computations are summarized in Table 5, where r represents the real part and r' the imaginary part of the refractive index, written $m = r - ir'$, and x_1 and x_2 represent the lower and upper limits of the relative size, respectively.

Table 5

Refractive Index		Limits of Size		Substance	Wavelength (μ)
r	r'	x_1	x_2		
1.111	0.1831	0.5	10.0	water	11.50
1.212	0.0601	0.5	10.0	water	10.00
1.29	0	0.5	30.0	water	2.25
	0.0472	0.5	12.0	water	8.15
	0.0645	0.5	18.0	.....	.....
	0.4720	5.25	10.0	.....	.....
1.315	0	0.5	40.0	water	1.61
	0.0143	0.5	15.0	water	5.30
	0.1370	0.5	15.0	water	6.05
	0.4298	0.5	10.0	water	15.00
1.34	0	0.5	70.0	water	0.45
1.353	0.0059	0.5	20.0	water	3.90
1.44	0	0.5	7.0	.....	.....
	0.4000	0.5	7.0	water	16.6
1.525	0	0.5	7.0	.....	.....
	0.0050	0.5	7.0	.....	.....
	0.0100	0.5	7.0	.....	.....
	0.0682	0.5	25.0	water	3.07
1.28	1.37	0.1	7.0	iron	0.441
1.51	1.63	0.1	7.0	iron	0.589
1.70	1.84	0.1	7.0	iron	0.668

The complete angular range from 0° to 180° was covered in steps of 5° or 2½°, except in the forward area between 0° and 15°, where the steps were made smaller to get the details of the aureole.

APPENDIX C

SELECTED COMPLEX AMPLITUDE VALUES

A TABULATION of the values of the complex amplitude S_1 at $\theta = 0°$ and 180° is presented in Table 6 for selected indices of refraction, as a function of x in steps of 0.5 in x. The six significant figures of the IBM printouts have been rounded off to four in this table.

Table 6

SCATTERING AMPLITUDE $S_1(\theta)$

x	$m = 1.315 - 0.0143i$		x	$m = 1.315 - 0.1370i$	
	$\theta = 0°$	180°		$\theta = 0°$	180°
0.5	$0.001486 + 0.02540i$	$0.001360 + 0.02276i$	0.5	$0.01088 + 0.02540i$	$0.009682 + 0.02278i$
1.0	$0.03134 + 0.2157i$	$0.02638 + 0.1356i$	1.0	$0.1135 + 0.1991i$	$0.07447 + 0.1217i$
1.5	$0.1987 + 0.7324i$	$0.1185 + 0.1706i$	1.5	$0.4621 + 0.6048i$	$0.1358 + 0.1190i$
2.0	$0.7173 + 1.708i$	$-0.01680 - 0.1694i$	2.0	$1.231 + 1.228i$	$-0.1113 - 0.04711i$
2.5	$1.830 + 3.010i$	$-0.5268 - 0.1889i$	2.5	$2.501 + 1.961i$	$-0.3722 + 0.006813i$
3.0	$3.712 + 4.697i$	$-0.09836 + 0.3335i$	3.0	$4.350 + 2.710i$	$-0.02972 - 0.007636i$
3.5	$6.495 + 6.328i$	$0.8710 - 0.2157i$	3.5	$6.745 + 3.355i$	$0.3093 - 0.3400i$
4.0	$10.37 + 7.883i$	$0.005407 - 0.7426i$	4.0	$9.649 + 3.775i$	$0.1557 - 0.1735i$
4.5	$14.98 + 8.961i$	$-0.7402 + 0.7945i$	4.5	$12.99 + 3.945i$	$0.09903 + 0.4225i$
5.0	$20.63 + 9.123i$	$0.5753 + 1.0090i$	5.0	$16.62 + 3.792i$	$0.03693 + 0.4169i$
5.5	$26.62 + 8.843i$	$0.1670 - 1.038i$	5.5	$20.52 + 3.352i$	$-0.3695 - 0.03435i$
6.0	$32.75 + 6.786i$	$-1.303 - 0.5803i$	6.0	$24.52 + 2.677i$	$-0.4403 - 0.3023i$
6.5	$39.27 + 4.603i$	$0.3777 + 0.6886i$	6.5	$28.64 + 1.782i$	$0.08278 - 0.3978i$
7.0	$44.20 + 0.8754i$	$1.343 - 0.4918i$	7.0	$32.79 + 0.8248i$	$0.5289 - 0.2107i$
7.5	$48.89 - 3.347i$	$-0.3750 - 0.009495i$	7.5	$36.99 - 0.2126i$	$0.4821 + 0.2665i$
8.0	$53.02 - 6.948i$	$-0.1797 + 1.261i$	8.0	$41.30 - 1.181i$	$-0.03776 + 0.5581i$
8.5	$56.16 - 12.18i$	$-0.1858 - 0.3840i$	8.5	$45.67 - 2.076i$	$-0.5840 + 0.3876i$
9.0	$58.58 - 14.34i$	$-1.491 - 0.4334i$	9.0	$50.24 - 2.861i$	$-0.5402 - 0.2128i$
9.5	$58.47 - 17.82i$	$0.8030 + 0.3386i$	9.5	$55.01 - 3.484i$	$-0.04274 - 0.7919i$
10.0	$61.26 - 18.79i$	$1.626 - 1.978i$	10.0	$60.05 - 4.019i$	$0.4350 - 0.5364i$
10.5	$60.21 - 17.41i$	$-1.526 - 0.1506i$	10.5	$65.42 - 4.406i$	$0.7286 + 0.3562i$
11.0	$63.14 - 17.57i$	$0.6679 + 3.602i$	11.0	$71.10 - 4.746i$	$0.3948 + 0.7659i$
11.5	$65.89 - 11.58i$	$2.639 - 0.9226i$	11.5	$77.17 - 5.027i$	$-0.6033 + 0.4945i$
12.0	$68.60 - 9.743i$	$-3.434 - 2.816i$	12.0	$83.57 - 5.302i$	$-1.027 - 0.02237i$
12.5	$77.51 - 3.590i$	$-2.343 + 3.477i$	12.5	$90.36 - 5.614i$	$-0.2722 - 0.7155i$
13.0	$82.33 + 2.087i$	$4.996 + 0.5374i$	13.0	$97.47 - 5.958i$	$0.5962 - 0.9706i$
13.5	$95.07 + 4.284i$	$-0.3004 - 4.936i$	13.5	$104.9 - 6.392i$	$0.8341 - 0.06801i$
14.0	$106.3 + 11.51i$	$-5.222 + 2.677i$	14.0	$112.6 - 6.887i$	$0.5670 + 1.032i$
14.5	$118.4 + 9.719i$	$3.034 + 4.282i$	14.5	$120.6 - 7.474i$	$-0.2645 + 0.9576i$
15.0	$135.9 + 12.26i$	$2.263 - 5.963i$	15.0	$128.9 - 8.130i$	$-1.159 + 0.03418i$

Table 6—*continued*

	$m = 1.315 - 0.4298i$			$m = 1.525 - 0.0682i$	
x	$\theta = 0°$	180°	x	$\theta = 0°$	180°
0.5	$0.03335 + 0.02740i$	$0.02964 + 0.02496i$	0.5	$0.005742 + 0.04069i$	$0.005107 + 0.03618i$
1.0	$0.2896 + 0.1609i$	$0.1752 + 0.09946i$	1.0	$0.1050 + 0.3485i$	$0.07900 + 0.2058i$
1.5	$0.9203 + 0.3406i$	$0.1784 + 0.09446i$	1.5	$0.6209 + 1.120i$	$0.2012 + 0.1065i$
2.0	$1.959 + 0.4904i$	$-0.1477 + 0.1436i$	2.0	$2.037 + 2.070i$	$-0.4206 - 0.1089i$
2.5	$3.378 + 0.5498i$	$-0.3402 + 0.1477i$	2.5	$4.310 + 3.059i$	$-0.3192 + 0.3349i$
3.0	$5.140 + 0.5060i$	$-0.1888 - 0.1756i$	3.0	$7.325 + 3.181i$	$0.3735 - 0.5663i$
3.5	$7.204 + 0.3515i$	$0.07502 - 0.4741i$	3.5	$11.17 + 2.700i$	$-0.3524 - 0.4348i$
4.0	$9.547 + 0.1074i$	$0.3292 - 0.2324i$	4.0	$14.43 + 1.589i$	$0.7267 + 0.7693i$
4.5	$12.14 - 0.2123i$	$0.4415 + 0.3208i$	4.5	$17.51 - 0.7878i$	$0.5179 - 0.3916i$
5.0	$15.00 - 0.5899i$	$0.1160 + 0.5640i$	5.0	$20.36 - 2.532i$	$-1.400 + 0.8049i$
5.5	$18.10 - 1.009i$	$-0.5083 + 0.3170i$	5.5	$21.63 - 4.022i$	$0.4738 + 0.8497i$
6.0	$21.46 - 1.463i$	$-0.7046 - 0.1995i$	6.0	$23.49 - 5.373i$	$-0.3537 - 2.080i$
6.5	$25.07 - 1.942i$	$-0.1474 - 0.6636i$	6.5	$25.57 - 4.675i$	$-1.350 + 0.3665i$
7.0	$28.94 - 2.447i$	$0.5861 - 0.6184i$	7.0	$27.63 - 3.857i$	$2.433 + 0.8166i$
7.5	$33.08 - 2.972i$	$0.7970 + 0.1123i$	7.5	$31.91 - 2.641i$	$0.2802 - 1.530i$
8.0	$37.48 - 3.519i$	$0.3270 + 0.8788i$	8.0	$36.83 - 0.7611i$	$-2.146 + 2.106i$
8.5	$42.14 - 4.086i$	$-0.4976 + 0.8161i$	8.5	$42.79 - 0.3052i$	$1.118 + 1.261i$
9.0	$47.06 - 4.674i$	$-1.009 - 0.06469i$	9.0	$50.11 - 0.2722i$	$-0.9858 - 2.949i$
9.5	$52.26 - 5.283i$	$-0.6047 - 0.9212i$	9.5	$56.89 - 1.206i$	$-1.799 + 0.2044i$
10.0	$57.71 - 5.913i$	$0.4898 - 0.9856i$	10.0	$63.78 - 3.439i$	$2.731 + 0.4632i$
10.5	$63.43 - 6.562i$	$1.214 - 0.1574i$	10.5	$70.16 - 5.564i$	$0.8498 - 1.412i$
11.0	$69.41 - 7.232i$	$0.7941 + 0.9229i$	11.0	$75.44 - 7.910i$	$-1.507 + 2.047i$
11.5	$75.65 - 7.920i$	$-0.4079 + 1.258i$	11.5	$80.62 - 9.851i$	$0.3778 + 1.490i$
12.0	$82.15 - 8.628i$	$-1.294 + 0.3918i$	12.0	$85.58 - 10.66i$	$-1.164 - 1.884i$
12.5	$88.92 - 9.354i$	$-1.043 - 0.9520i$	12.5	$90.71 - 10.86i$	$-1.335 - 0.7169i$
13.0	$95.95 - 10.10i$	$0.2057 - 1.471i$	13.0	$96.85 - 10.38i$	$1.843 - 0.4074i$
13.5	$103.2 - 10.86i$	$1.382 - 0.6096i$	13.5	$103.9 - 9.411i$	$1.406 - 0.5205i$
14.0	$110.8 - 11.64i$	$1.344 + 0.8754i$	14.0	$112.0 - 8.704i$	$-0.1020 + 1.695i$
14.5	$118.6 - 12.43i$	$-0.0009 + 1.627i$	14.5	$121.0 - 8.487i$	$-0.4988 + 1.460i$
15.0	$126.6 - 13.24i$	$-1.448 + 0.9061i$	15.0	$130.6 - 8.859i$	$-1.584 - 0.4902i$

Table 6—*continued*

x	$m = 1.525 - 0.0682i$ (*continued*)	
	$\theta = 0°$	180°
15.5	$140.3 - 10.08i$	$-0.9278 - 1.293i$
16.0	$149.9 - 11.87i$	$0.9408 - 1.477i$
16.5	$159.0 - 13.85i$	$1.619 - 0.08854i$
17.0	$167.8 - 15.84i$	$1.213 + 1.515i$
17.5	$176.4 - 17.44i$	$-0.7231 + 1.460i$
18.0	$185.0 - 18.42i$	$-2.079 + 0.6153i$
18.5	$193.9 - 18.93i$	$-0.9834 - 1.289i$
19.0	$203.5 - 18.97i$	$0.3421 - 2.359i$
19.5	$213.7 - 18.91i$	$1.579 - 0.3918i$
20.0	$224.8 - 18.81i$	$2.105 + 1.446i$
20.5	$236.5 - 19.07i$	$-0.2199 + 1.670i$
21.0	$248.6 - 19.81i$	$-2.337 + 1.281i$
21.5	$260.9 - 21.03i$	$-1.589 - 0.8669i$
22.0	$273.2 - 22.55i$	$-0.1039 - 2.716i$
22.5	$285.4 - 24.25i$	$1.545 - 1.260i$
23.0	$297.4 - 25.89i$	$2.502 + 1.097i$
23.5	$309.4 - 27.29i$	$0.5882 + 2.124i$
24.0	$321.6 - 28.38i$	$-2.050 + 1.803i$
24.5	$334.0 - 29.14i$	$-2.381 - 0.3930i$
25.0	$346.9 - 29.65i$	$-0.8071 - 2.615i$

x	$m = 1.353 - 0.0059i$	
	$\theta = 0°$	180°
0.5	$0.0009267 + 0.02831i$	$0.0008735 + 0.02534i$
1.0	$0.03100 + 0.2433i$	$0.02807 + 0.1523i$
1.5	$0.2215 + 0.8316i$	$0.1414 + 0.1796i$
2.0	$0.8590 + 1.938i$	$-0.05711 - 0.2333i$
2.5	$2.183 + 3.330i$	$-0.6465 - 0.1145i$
3.0	$4.508 + 5.086i$	$0.1116 + 0.4448i$
3.5	$7.713 + 6.584i$	$0.9990 - 0.5862i$
4.0	$12.27 + 7.678i$	$-0.5021 - 0.6901i$

x	$m = 1.353 - 0.0059i$ (*continued*)	
	$\theta = 0°$	180°
4.5	$17.37 + 8.242i$	$-0.5012 + 1.520i$
5.0	$23.18 + 7.123i$	$1.208 + 0.4746i$
5.5	$29.58 + 5.744i$	$-0.8207 - 1.640i$
6.0	$34.40 + 2.427i$	$-1.617 + 0.4937i$
6.5	$40.53 - 1.806i$	$1.676 + 0.3686i$
7.0	$43.30 - 5.077i$	$0.8242 - 1.748i$
7.5	$46.23 - 11.31i$	$-0.8989 + 0.9890i$
8.0	$48.66 - 13.19i$	$1.247 + 1.448i$
8.5	$46.74 - 17.03i$	$-0.5544 - 1.082i$
9.0	$49.39 - 18.73i$	$-1.583 + 1.140i$
9.5	$47.17 - 15.09i$	$1.992 + 0.2156i$
10.0	$48.27 - 16.29i$	$-0.7223 - 2.425i$
10.5	$53.39 - 8.443i$	$-2.706 + 3.121i$
11.0	$52.81 - 4.671i$	$3.033 + 1.820i$
11.5	$64.56 - 0.1985i$	$-1.896 - 5.573i$
12.0	$70.96 + 10.49i$	$-6.221 + 0.2844i$
12.5	$82.83 + 8.538i$	$5.192 + 2.232i$
13.0	$100.55 + 14.84i$	$5.642 - 8.895i$
13.5	$108.5 + 14.24i$	$-4.756 - 0.4685i$
14.0	$129.6 + 8.984i$	$4.996 + 10.04i$
14.5	$142.5 + 10.19i$	$8.741 - 1.470i$
15.0	$152.5 - 5.353i$	$-7.987 - 2.797i$
15.5	$167.2 - 10.16i$	$-3.992 + 11.53i$
16.0	$168.2 - 17.68i$	$7.156 + 0.9539i$
16.5	$180.4 - 30.97i$	$-5.937 - 7.374i$
17.0	$182.6 - 33.07i$	$-10.87 + 6.522i$
17.5	$177.3 - 42.54i$	$3.894 + 2.975i$
18.0	$183.0 - 39.25i$	$-1.557 - 11.75i$
18.5	$179.9 - 33.88i$	$-7.989 - 4.519i$
19.0	$186.3 - 38.01i$	$6.125 + 0.5754i$
19.5	$190.2 - 24.66i$	$8.051 - 8.074i$
20.0	$193.5 - 16.42i$	$-0.4077 - 1.132i$

REFERENCES

1. VAN DE HULST, H. C., *Light Scattering by Small Particles*, John Wiley & Sons, Inc., New York, 1957.
2. JOHNSON, J. C., AND J. R. TERRELL, "Transmission Cross Sections for Water Spheres Illuminated by Infrared Radiation," *J. Opt. Soc. Am.*, Vol. 45, No. 6, June, 1955, pp. 451–454.
3. DEIRMENDJIAN, D., *Atmospheric Extinction of Infrared Radiation*, The RAND Corporation, Paper P-1880, January 7, 1960; also published in *Quart. J. Roy. Met. Soc.*, Vol. 86, No. 369, July, 1960, pp. 371–381.
4. DUFAY, J., *Galactic Nebulae and Interstellar Matter*, Philosophical Library, Inc., New York, 1957.
5. TWERSKY, V., "Electromagnetic Waves" (conference report), *Physics Today*, Vol. 13, No. 7, July, 1960, pp. 30–36.
6. SAXON, D. S., Z. SEKERA, AND D. DEIRMENDJIAN, *Approximation of Light Scattering by Large Dielectric Spheres*, Dept. of Meteorology, University of California, Los Angeles, Calif., Scientific Report 3 (AFCRC-TN-60-486), June, 1960.
7. DEIRMENDJIAN, D., *Theory of Solar Aureole—Part I: Scattering and Radiative Transfer*, The RAND Corporation, Research Memorandum RM-2008 (ASTIA No. AD 144282), October 3, 1957; also published in *Ann. Geophys.*, Vol. 13, No. 4, October–December, 1957, pp. 286–306.
8. DEIRMENDJIAN, D., *Theory of Solar Aureole—Part II: Applications to Atmospheric Models*, The RAND Corporation, Research Memorandum RM-2133 (ASTIA No. AD 156039), February 20, 1958; also published in *Ann. Geophys.*, Vol. 15, No. 4, April–June, 1959, pp. 218–249.
9. DEIRMENDJIAN, D., *On the Role of Clear Sky Turbidity in Atmospheric Infrared Transmission*, The RAND Corporation, Paper P-1565, December 3, 1958; also published in *Quart. J. Roy. Met. Soc.*, Vol. 85, No. 366, October, 1959, pp. 404–411.
10. SEKERA, Z., *Extension of the "WKB" Approximation of High-frequency Scattering by a Dielectric Sphere—Part I: General Expressions*, The RAND Corporation, Research Memorandum RM-2502 (ASTIA No. AD 245101), June 30, 1960.
11. PENNDORF, R., *Research on Aerosol Scattering in the Infrared: Scattering Coefficients for Absorbing and Nonabsorbing Aerosols*, Avco Corp., Wilmington, Mass., Scientific Report 3 (AFCRL-TN-60-667), October, 1960.
12. LOWAN, A. N., *Tables of Scattering Functions for Spherical Particles*, National Bureau of Standards, Washington, D.C., Applied Mathematics Series 4, 1949.

13. HAUGEN, D. A., "On the Scattering of Light by Spherical Absorbers," unpublished M.S. thesis, Massachusetts Institute of Technology, 1952.

14. WATSON, G. N., *A Treatise on the Theory of Bessel Functions*, 2d ed., The Macmillan Co., New York, 1944.

15. PENNDORF, R., AND B. GOLDBERG, *New Tables of Mie Scattering Functions for Spherical Particles*, A. F. Cambridge Research Center, Bedford, Mass., Geophysical Research Papers 45, Parts 3 and 6 (ASTIA No. AD 98769 and AD 98772), March, 1956.

16. CENTENO, M., "The Refractive Index of Liquid Water in the Near Infra-Red Spectrum," *J. Opt. Soc. Am.*, Vol. 31, No. 3, March, 1941, pp. 244–247.